MAGNETIC PROPERTIES OF LAYERED HEXAGONAL COBALT HYDROXIDE AND NICKEL HYDROXIDE NANOPARTICLES

A Thesis Submitted
in partial fulfillment of the requirements
for the degree of
Doctor of Philosophy

by
Anu Gupta
(Regn. No. 901212002)

Under the Supervision of
Dr. S. D. Tiwari
(Associate Professor)

THAPAR INSTITUTE
OF ENGINEERING & TECHNOLOGY
(Deemed to be University)

to the
SCHOOL OF PHYSICS AND MATERIALS SCIENCE
THAPAR INSTITUTE OF ENGINEERING AND TECHNOLOGY, PATIALA 147004
INDIA
August 2018

DECLARATION

I hereby certify that work presented in this thesis entitled "*Magnetic Properties of Layered Hexagonal Cobalt Hydroxide and Nickel Hydroxide Nanoparticles*" in partial fulfillment of the requirement of the award of degree of DOCTOR OF PHILOSOPHY in the School of Physics and Materials Science, Thapar Institute of Engineering and Technology, Patiala is an authentic record of my own work carried out under supervision of Dr. S. D. Tiwari. The matter embodied in this thesis has not been submitted in part or full to any other university or institute for the award of any degree.

Anu Gupta

This is to certify that the above statement made by the candidate is true to the best of my knowledge.

Dr. S. D. Tiwari
Associate Professor
School of Physics and Materials Science
Thapar Institute of Engineering and Technology
Patiala

SYNOPSIS

Transition metal hydroxides are interesting systems and have many important technological applications. Among these, cobalt hydroxide and nickel hydroxide are of more interest. Cobalt hydroxide is found to be useful for future magnetic refrigeration systems based on magnetocaloric effect whereas nickel hydroxide has already been in extensive use in rechargeable batteries. These materials exist in alpha and beta phases having layered hexagonal structures. The alpha phase is an unstable system. Both phases mainly differ in value of lattice parameter c. Magnetic behavior of cobalt hydroxide and nickel hydroxide could not attract the attention of researchers much despite of being such interesting systems. This thesis presents a detailed magnetic investigations on alpha and beta phases of cobalt hydroxide and nickel hydroxide nanoparticles. An outline of the thesis is as follows.

Chapter 1 contains introduction of the work. It begins with origin of magnetism in solids. Change in behavior of materials due to finite size effect, importance of the work, motivation behind presented work are discussed followed by a review of the literature.

Chapter 2 describes synthesis of alpha and beta phases of cobalt hydroxide and nickel

hydroxide nanoparticles. It also discusses the working principles of x-ray diffractometer, Fourier transform infrared spectrometer, thermogravimetric analyzer and vibrating sample magnetometer.

Chapter 3 describes characterization of undoped, 10 and 20% Al doped alpha cobalt hydroxide nanoparticles. Molecular formula of each sample is estimated with help of FTIR spectra and thermogravimetric analysis. The system decomposes to spinel $CoO{\cdot}Co_{2-3x}Al_{3x}O_3$ on heating in air. Fitting of susceptibility versus temperature data (5-300 K) in 500 G applied magnetic field indicates for ferromagnetic transition in the system at lower temperatures. The Curie transition temperature decreases with increasing concentration of Al in the lattice. Superparamagnetic blocking of particle magnetic moment is observed below the Curie temperature. M-B loop data at 300 and 5 K are also presented to support the outcome of analysis.

Chapter 4 describes characterization of beta cobalt hydroxide nanoparticles. It decomposes to Co_3O_4 on heating in air. ZFC and FC susceptibility versus temperature (5-300 K) curve in 500 G applied magnetic fields are seen to bifurcate at 11 K. This bifurcation temperature is independent of applied magnetic field strength and represents the Néel temperature of the system. Strength of one strong intraplaner ferromagnetic exchange interaction and two weak interplaner antiferromagnetic interactions among Co^{2+} ions are also estimated.

Chapter 5 describes characterization of undoped, 10 and 20% Al doped alpha nickel hydroxide nanoparticles. Molecular formula of samples are estimated with help

of FTIR spectra and thermogravimetric analysis. Samples decompose to cubic $Ni_{1-x}Al_xO_{1+\frac{x}{2}}$ on heating in air. Analysis of ZFC and FC susceptibility data in different applied magnetic field strength indicate that all samples undergo ferromagnetic transitions at different temperatures followed by superparamagnetic blocking of particle magnetic moment. M-B loop data at 300 and 5 K are also presented.

Chapter 6 describes characterization of beta nickel hydroxide nanoparticles. It decomposes to NiO on heating in air. ZFC and FC susceptibility versus temperature (5-300 K) curves in different applied magnetic field always bifurcate at 21 K. This bifurcation temperature represents the Néel temperature of the system. Strength of three possible exchange interactions among Ni^{2+} ions in such systems are also estimated.

Chapter 7 concludes the thesis. It also contains scope for future work.

ACKNOWLEDGEMENTS

It is my privilege to owe my gratitude to all those who have been with me during this thesis work. First of all, I thank my thesis supervisor Dr. S. D. Tiwari for his support, guidance, suggestions and encouragement throughout the course of this work. It was very difficult to complete this work without his support.

I thank Dr. O. P. Pandey, Dean of Research and Sponsored Projects, for his support and extensive help. I acknowledge Dr. Kulvir Singh for encouraging me in several ways. I thank Dr. Manoj Sharma, Head of the School, for his kind help and cooperation.

I express my sincere thanks to other doctoral committee members Dr. B. C. Mohanty and Dr. Bonamali Pal for their suggestions and comments. I acknowledge Dr. B. N. Chudashama for characterizing the samples with TGA. Other faculty members of the School are also thankfully acknowledged for their cooperation.

I would also like to acknowledge my fellow colleagues for their cordial help, moral support and valuable information during the hard time of this thesis work. Staff members of SAI Lab are also acknowledged for their technical help and cooperation.

Lastly, I must acknowledge my family members for their affection and unfailing support. I express a special thanks to my loving daughter Angel.

Anu Gupta

CONTENTS

LIST OF FIGURES

LIST OF TABLES

LIST OF ABBREVIATIONS

XRD	X-ray diffraction
nm	Nanometer
ZFC	Zero field cooled
FC	Field cooled
emu	Electromagnetic unit
g	Gram

LIST OF NOTATIONS

M	Magnetization
B	Magnetic induction
χ	Susceptibility
T	Temperature
T_{bf}	Bifurcation temperature
T_B	Blocking temperature
N	Number of ions per unit mass
μ	Ionic magnetic moment
k_B	Boltzmann constant

Chapter 1

INTRODUCTION

1.1 Magnetism in Solids

A very large number of atoms or ions come close to one another and arrange themselves in a well defined periodic manner in three dimension to form crystalline solids [1–3]. Mostly solids exist in crystalline form as this form posses minimum configuration energy. Therefore, this state of solids is most stable form. Atoms consist of negatively charged electrons and positively charged nucleus. Electrons and nucleons are always in state of rotational motion. Such rotation of charged particles always produces a magnetic moment. The nuclear contribution of magnetic moment is much smaller and becomes significant only at very low temperatures. In this way orbital motion and spin of electrons in atoms are mainly responsible for origin of magnetism in solids.

Solids consisting of only paired electrons always oppose the effect of external applied magnetic field because of Lenz's law. Such solids are termed as diamagnetic materials. Susceptibility of these materials are independent of temperature. Only atoms consisting of unpaired electrons can have a net magnetic moment. A collection of such non-interacting atoms or ions forms paramagnetic solids. In the absence of field, moments are aligned randomly in these solids. These moments try to align themselves along the field direction when placed in external magnetic field. The susceptibility χ of the

system varies with temperature T according to the relation

$$\chi = \frac{C}{T}, \tag{1.1}$$

where C is a material dependent constant. This is known as Curie's law. On other hand, if the interaction among the moments becomes significant then these moments may arrange themselves in ferro, ferri or antiferromagnetic ordering below a critical temperature. Behavior of ferro, ferri and antiferromagnetic materials well above the ordering temperature is somewhat similar to paramagnetic materials and susceptibility

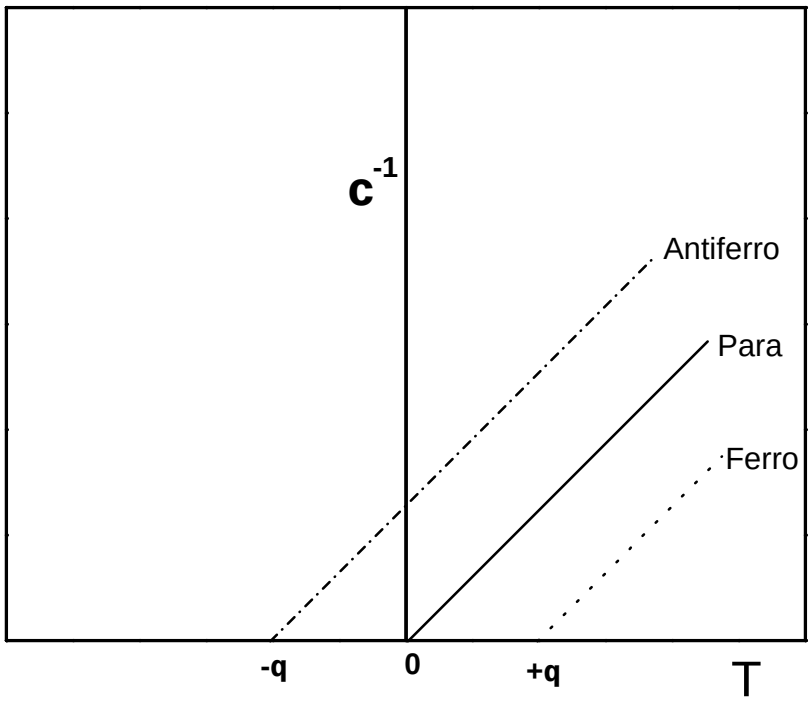

Fig. 1.1: Inverse susceptibility as a function of temperature for different magnetic materials.

of these materials in high temperature region is given by relation

$$\chi = \frac{C}{T - \theta}. \tag{1.2}$$

Here, parameter θ is positive for ferromagnetic interactions and negative for antiferromagnetic interactions. Its magnitude, usually, represents corresponding ordering temperature. The nature of significant magnetic interaction in any solid can easily be characterized by plotting χ^{-1} vs. T. These plots for para, ferro and antiferromagnetic materials are shown in Fig. 1.1.

1.2 Magnetic Interactions

In ferromagnetic materials, all magnetic moments are aligned in same direction. There are many theories to explain behavior of ferromagnetic materials [4, 5]. In 1907, Pierre Weiss found that there exist a strong internal magnetic field produced by magnetic ions inside the solid. The origin of this field was not known. Later on, a concept of quantum mechanical exchange interaction among spins was introduced. This interaction is very strong but short range in nature. In 1925, Ising model was proposed by Ernst Ising. In this model neighboring spins may be either parallel or antiparallel to each other. He solved the model for one dimensional case and concluded that no ferromagnetic transition can occurs. This led to failure of Ising model. It has been concluded that no ferromagnetic transition is possible for two and three dimensional lattices also. A breakthrough to this conclusion was made by Lars Onsager in 1944. He provided an exact solution to two dimensional Ising model using transfer matrix method. Till now, no exact solution has been proposed for three dimensional Ising lattice. In 1971, K. Wilson developed computer simulation and approximate method that can provide fairly good result for three dimensional lattices. The discrepancy of the Ising model was considered by Heisenberg. In 1928, he proposed an updated version which is

completely based on the quantum physics. Unlike Ising model, this model takes all possible spin orientations into consideration. Clearly, the Ising model is special case of the Heisenberg model.

Ising type model can be further simplified with high temperature series expansion, low temperature series expansion and density expansion methods. At high temperature, all the spins are randomly aligned and partition function is same for ferro and antiferromagnets in absence of any external magnetic field. But this is not the case in presence of any applied field. Series for ferro and antiferromagnets have different sign for exchange coefficients. But the case is different for low temperature series expansion. Here, spins are aligned even in the absence of any external magnetic field. In density approximation two different types of parameters are required in series expansion.

The series expansion method is considered to be best one as it provides exact information about critical phenomena. The results obtained from the series expansion are applicable below, at or above the transition temperature whereas results of renormalization group are valid only in the critical region.

1.3 Nanomagnetism

Researchers from different disciplines have been studying magnetic behavior of fine particles. Behavior of these materials is different from corresponding bulk form [6–8]. People have different reasons for their interest in these materials. For physicists, particularly, the interest in small particles of magnetic materials is because of interesting behavior shown by them. Superparamagnetism is only shown by these systems [9].

Magnetization vector of ferro and ferrimagnetic crystals is easily directed along a preferred crystallographic axis [10]. This direction is called easy axis. On other hand, there is also an axis along which the alignment of magnetization vector is most difficult. This is called hard axis. The rotation of magnetization vector is possible with help of an applied magnetic field. Uniaxial anisotropy is simplest type of anisotropy. In

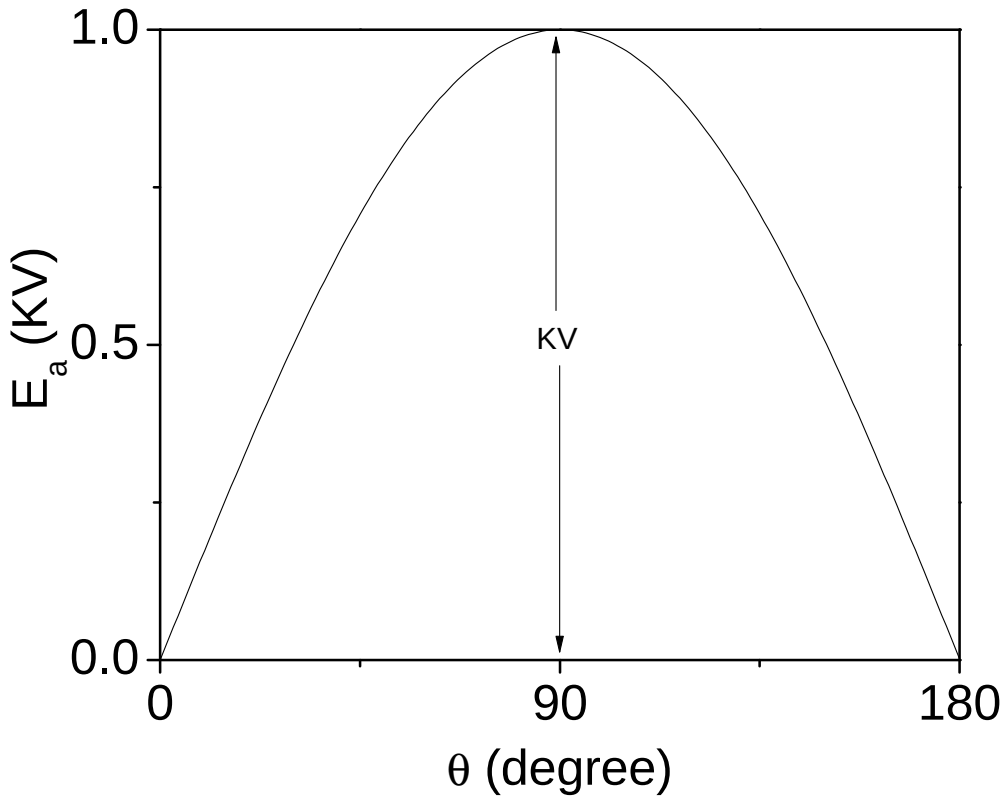

Fig. 1.2: Variation of magnetocrystalline anisotropy energy E_a as a function of angle θ for an uniaxial crystal.

this, only one direction is there for orientation of magnetization vector. Hexagonal cobalt is a good example of such system. The easy axis is the c axis and hard axis is perpendicular to this.

The magnetocrystalline anisotropy energy for uniaxial systems is written as

$$E_a \approx KV \sin^2 \theta, \tag{1.3}$$

where K is anisotropy constant and V is volume of crystal. Figure 1.2 shows a plot of anisotropy energy as a function of angle θ. The energy barrier KV can be overcome with help of applied magnetic field or by increasing the temperature of system. If

anisotropy energy becomes less than the thermal energy then the magnetization vector will no longer be fixed in direction and starts flipping between two orientations of minimum energy with frequency

$$\nu = \nu_0 e^{-\frac{KV}{k_B T}}, \tag{1.4}$$

where ν_0 is a constant. This relation is known as Arrhenius law [9]. This situation is similar to paramagnetism and termed as superparamagnetism.

1.4 Applications of Nanomaterials

Nanomaterials also have many useful applications in areas of science and engineering apart from exhibiting interesting behavior. Few important applications of nanomaterials are described below.

1.4.1 Nanofluids

Nanofluids are suspension of nano sized particles in liquids [11]. Most important nanofluids are magnetic nanofluids and thermal nanofluids. Magnetic nanofluids are suspension of ferro and ferrimagnetic particles. These particles may be functionalized with molecules of appropriate drugs for targeted delivery [12]. In this delivery method, only small amount of medicine is injected at affected part of the body. This limits the exposure of drug to whole body and associated side effects. Ferrofluids are also used to kill cancer cells inside body. For this, the suspension of superparamagnetic particles is first injected at affected area. After this, an external alternating magnetic field is applied. This causes generation of heat and an increase in the temperature of cells. The cancer cells are more susceptible to heat and are killed first without affecting normal cells [13].

Nanofluids containing suspension of suitable materials can also be used to control

rate of heat transfer from a system [14]. This results in great energy savings in industrial cooling applications. Use of indium nanoparticles has been found to enhance specific heat and thermal conductivity of nanofluids. There is a potential application of such fluid in enhancing cooling rate of transformers [15]. For this magnetic nanoparticles of appropriate transition temperature are dispersed in the oil. When these nanoparticles approaches the coil, its temperature rises and particles loss their magnetization. This creates a gradient in density and fluid magnetization. In this manner, an additional heat flow is added due to thermo-magnetic convection.

1.4.2 Magnetic recording

Fine particles of magnetic materials are used for data storage applications [16]. Small size of particles increases storage density. But at same time particles should be sufficiently large so that the system does not remain in superparamagnetic region. One bit of information can be stored in each particle by orienting particle magnetization in specific direction with help of an external applied magnetic field. This magnetic field is applied by a current carrying coil called recording head. The stored information is detected by another pick up coil called read head. Sizes of magnetic particles, recording and read heat are very important and which finally decide the overall storage density of the device.

1.4.3 Catalysts

Rate of chemical reaction is enhanced by the use of catalyst [17]. Chemical reactions take place at the surface. Nanomaterials have high surface to volume ratio. Due to this nanomaterials are considered to have better catalytic activities. These nanocatalysts are used in different chemical reactions including in automobile catalytic converters for the removal of noxious and toxic gases such as carbon monoxide and nitrogen oxide [18]. These are also used in power generation equipments to prevent environmental pollution

arising from burning of gases and coal.

1.4.4 Mechanical tools

Fast development of machinery requires development of new tool materials. Machining tools must have high wear resistance [19]. Combination of increased hardness, toughness and wear-resistance of tool materials is the main goal. Nanostructured alloys and composite materials with nanosized structural constituents have these characteristics. These materials improve their mechanical properties as well as modify their thermal conductivity and corrosion resistance. Nanostructures of tungsten carbide, tantalum carbide and titanium carbide are examples of such materials. Nanostructured wear resistant coatings are also used to enhance the performance of cutting tools. Multilayer and multicomponent coatings have the highest mechanical properties, wear resistance and adhesion to the substrate [20].

1.4.5 Antibacterial activity

Infections to human are caused by bacteria. It can be prevented with help of many available antibiotics. Although these antibiotics are quite cheap but have side effects. A new approach involving nanoparticles of suitable materials have been developed to control the activity of bacterial growth [21]. These materials break the cell membrane of bacteria. Now metal ions react with respiratory enzymes of bacteria and results in oxidation of respiratory enzymes and produce reactive oxygen species of various kinds. This results in death of bacteria. The most commonly used nanoparticles for antibacterial activities are of copper, silver, gold etc.

1.5 Motivation, Objectives and Literature Review

Among different transition metal hydroxides, nickel hydroxide and cobalt hydroxide are interesting systems. Mostly, these materials are used in rechargeable batteries [22–24].

Structure and morphology of these materials are known to affect its performance in batteries. Due to this, there have been extensive works on different routes of their synthesis and structural characterization. These materials have hexagonal layered structure and crystallize in two phases known as alpha and beta [25, 26]. Both phases mainly differ in value of lattice parameter c. It is much larger for the alpha phase due to incorporation of extra hydroxyl groups and other anions during synthesis. The alpha phase is unstable in nature but shows superior electrochemical behavior [22, 27]. To utilize the potential of this phase, there have been a lot of efforts to stabilize the alpha phase by partial substitution of nickel ions in lattice by several other metal ions without affecting its electrochemical behavior much [22–24]. Trivalent Al^{3+} are found to be most effective for this purpose [22]. Despite of being such important and interesting systems, magnetic behavior of cobalt hydroxide and nickel hydroxide could not attract the attention of researchers much.

In 1966, Takada *et* al. published brief reports on magnetic behavior of cobalt hydroxide and nickel hydroxide [28,29]. Materials are reported to be antiferromagnetic in these works. But the analysis of χ vs. T curve indicates for ferromagnetic interaction in the system. In 1971, Szytula *et* al. reported neutron diffraction study on beta nickel hydroxide [30]. It was found that magnetic moments of Ni^{2+} ions in each layer are aligned ferromagnetically along the c-axis and neighboring layers are ordered antiferromagnetically. Following this work, the beta cobalt hydroxide is also considered to have similar magnetic structure. In 2008, Tiwari and Rajeev reported a detailed magnetic investigation on beta nickel hydroxide [31]. In this work the interaction among Ni^{2+} ions is once again found to be ferromagnetic. At same time, Liu *et* al. studied magnetic properties of beta cobalt hydroxide followed by another independent work by Shamba *et* al. in 2010 [32,33]. In both works, beta cobalt hydroxide is found to exhibit magnetocaloric effect. This observation is claimed to be useful for future refrigeration systems. In 2011, Neilson *et* al. studied magnetic properties of alpha cobalt hydrox-

ide [34]. The magnetic properties of alpha nickel hydroxide is never studied before. Effect of Al doping on magnetic properties of cobalt hydroxide and nickel hydroxide is also never studied. These issues motivated me to work on these systems. Objectives of this thesis are:

1. Synthesis of alpha and beta phases of cobalt hydroxide and nickel hydroxide nanoparticles by chemical methods.

2. Structural and thermal characterization of synthesized samples.

3. Analysis of magnetization data to study and compare magnetic behavior of samples.

In 2010, Rall *et* al. studied and compared magnetic properties of bulk and nanoplate like beta nickel hydroxide [35]. In this work the material is found to be an overall antiferromagnet. A high strength applied magnetic field induces a transition to ferromagnetic state. This group also presented a study of magnetic properties of alpha and beta phases of nickel hydroxide [25, 36]. The alpha phase is found to be a hard ferromagnet whereas the beta phase is once again found to be an overall antiferromagnet.

Chapter 2

EXPERIMENTAL DETAILS

In this chapter synthesis of alpha and beta phases of cobalt hydroxide and nickel hydroxide is presented. Working principles of used characterization techniques are also discussed.

2.1 Synthesis

Many physical and chemical methods have been developed for synthesis of nanomaterials [7]. In this work, chemical routes for synthesis of materials are used because these are low cost and convenient. Chemical reactions take place at atomic level. Due to this size and shape of particles during synthesis can easily be controlled following chemical methods. Chemicals required for synthesis are purchased from Sigma-Aldrich Corporation, USA. Laboratory prepared triple distilled water is used.

α **Cobalt Hydroxide:** 2.935 g $Co(NO_3)_2{\cdot}6H_2O$ is dissolved in 100 ml of ethylene glycol in a glass beaker under sonication. After this 100 ml of distilled water is added to the solution and then the beaker is kept on a magnetic stirrer. Now ammonia solution is added to the system drop wise till pH reaches 7.5. The resulting solution is kept at 50 ^{0}C for 2 hours and then allowed to cool at room temperature [37]. 10 and 20% Al doped α cobalt hydroxide nanoparticles are also synthesized. For this, the original solution contains Co^{2+} and Al^{3+} ions in appropriate amount whereas rest of steps remain unchanged. Dark brown precipitates are washed many times with distilled

water, dried under vacuum and ground.

β **Cobalt Hydroxide:** 4 M aqueous solution of sodium hydroxide is added to a 0.5 M aqueous solution of cobalt (II) nitrate hexahydrate under continuous stirring till the pH of the system reaches to 12 [32]. Pink precipitate is washed many times with distilled water, dried under vacuum and ground. Al doped β cobalt hydroxide nanoparticles could not be synthesized because any such attempt always stabilizes the system into α-phase.

α **Nickel Hydroxide:** Ammonium hydroxide solution is added drop wise to a 0.5 M aqueous solution containing Ni^{2+} and Al^{3+} ions in appropriate amount at 4 ^{0}C while continuously stirring till pH of system reaches 10 [38]. This mixture is aged at same temperature for 18 hours. Green precipitates are washed many times with distilled water, dried under vacuum and ground.

β **Nickel Hydroxide:** 4 M aqueous solution of sodium hydroxide is added to a 0.5 M aqueous solution of nickel (II) nitrate hexahydrate under continuous stirring till the pH of the system reaches to 12 [39]. Green precipitate is washed many times with distilled water, dried under vacuum and ground. Al doped β nickel hydroxide nanoparticles could not be synthesized because any such attempt always stabilizes the system into α-phase.

2.2 Experimental Techniques

2.2.1 X-ray diffraction

X-ray diffraction technique is used to identify phase of crystalline material. Crystals are composed of parallel atomic planes. A monochromatic beam of incident x-ray of wavelength λ undergoes Bragg diffraction if

$$2dSin\theta_B = n\lambda. \tag{2.1}$$

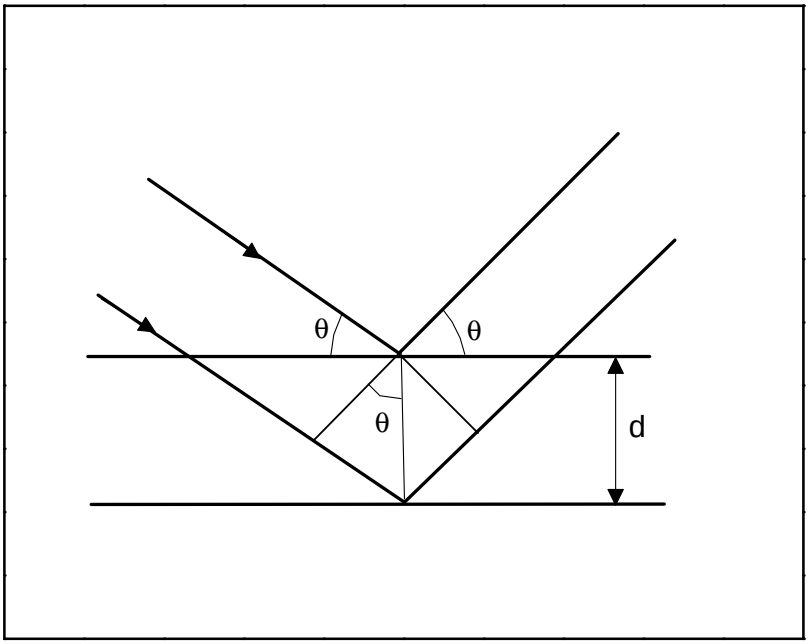

Fig. 2.1: Diffraction of x-ray beam from parallel atomic planes.

Here $n = 1, 2, ...$ and θ_B is Bragg's angle. The situation is described in Fig. 2.1. Grains in powder samples are randomly oriented and so all possible crystal orientations can be accessed simultaneously. Therefore, we get several diffraction peaks, corresponding to each d value, in x-ray diffraction pattern of a powder sample. Phase of a given material can be easily identified with help of this unique diffraction pattern.

X-ray diffraction peaks for a bulk powder sample are extremely sharp but always have finite broadening because of instrument, lattice strain and crystallite size. Full width at half maximum B of the line broadening and crystallite size t are related as

$$t = \frac{0.9\lambda}{BCos\theta_B}. \tag{2.2}$$

This relation is known as Scherrer formula [40]. Full width at half maximum of same peak in x-ray diffraction pattern of bulk standard powder sample is subtracted from that of sample to avoid effect of instrumental broadening. In this study x-ray diffraction data are collected using a PANalytical x-ray diffractometer using CuK_{α} radiation at room temperature. Polycrystalline silicon powder is used as a standard sample.

2.2.2 Fourier transform infrared spectrometer

Molecules consist of several bonds. These bonds are always formed between two atoms. Exact number of bonds depends on number of atoms in the molecule. These bonds are always in state of anharmonic oscillations with characteristic frequencies. The vibrational frequencies of bonds lie in infrared region of electromagnetic waves. Molecules may go to higher vibrational state by absorbing infrared radiation of appropriate frequencies. This is origin of vibrational or infrared spectroscopy [41]. Just by taking the Fourier transform of the observed infrared spectra one can easily get many other useful information about the molecule from same spectra in short time with improved resolution. These information include compound identification, structural elucidation, quantitative analysis, measurement of fundamental properties of a molecules etc [42]. In this work FTIR spectra of samples are collected using Perkin Elmer Spectrum RX-1 in transmission mode.

2.2.3 Thermogravimetric analyzer

Thermogravimetric analyzer is used to check the stability of materials at higher temperatures [43]. In this technique, mass of sample is recorded as a function of temperature while heating the sample at a constant heating rate in air or any other specific environment. In this work a NETZSCH STA 449F3 thermogravimetric analyzer is used. The data are recorded at constant heating rate of 5 ^{0}C per minute using alumina crucible and air atmosphere.

2.2.4 Vibrating sample magnetometer

Faraday's law of electromagnetic induction is used to measure magnetization of samples in vibrating sample magnetometer [44]. The sample is magnetized by application of an external magnetic field. The external magnetic field is generated by an electromagnet or a superconducting coil. Then the sample is made to vibrate inside a copper coil, called pick up coil, at a particular frequency. Due to this, magnetic flux passing through the coil changes and induces an emf, which is proportional to the magnetization. After suitable calibration, the variation in magnetization can be measured as function of temperature and applied magnetic field.

In present work, a commercial vibrating sample magnetometer (Quantum Design,

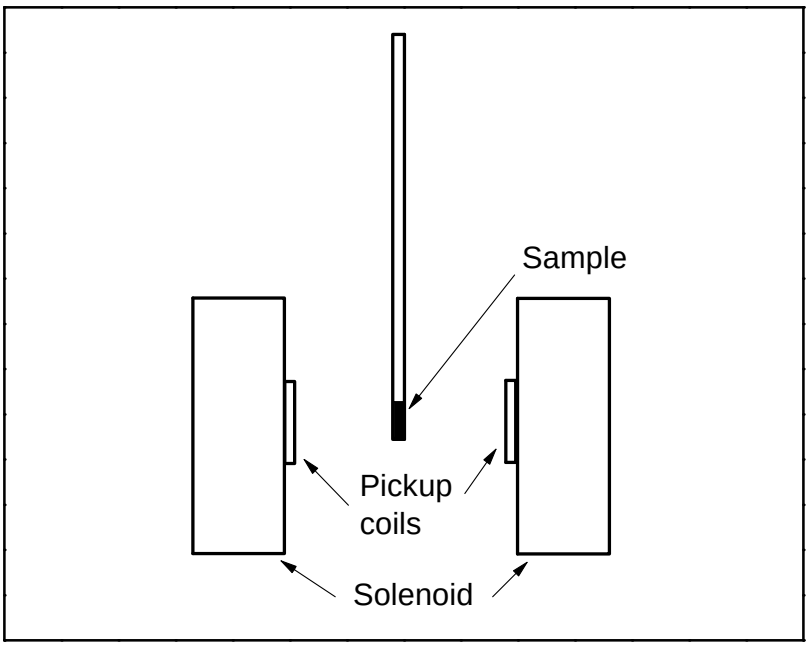

Fig. 2.2: Arrangement of superconducting solenoid, pick up coil and sample in a vibrating sample magnetometer.

PPMS) is used. The powder sample is tightly packed inside a perspex capsule to measure magnetization as function of temperature and applied magnetic field.

Chapter 3

ALPHA COBALT HYDROXIDE NANOPARTICLES

In this chapter structural, thermal and magnetic characterization of undoped and Al doped alpha cobalt hydroxide nanoparticles are presented.

3.1 Structural Characterization

Room temperature XRD patterns of undoped, 10 and 20% Al doped cobalt hydroxide nanoparticles are shown in Fig. 3.1. The patterns confirm the formation of single phase α cobalt hydroxide [26]. Broadening in the peaks indicates for nanocrystalline nature of samples. Average crystallite size, using Scherrer formula, comes out to be about 15 nm. Values of lattice parameters a and c of hexagonal unit cell are estimated to be 3.08(1) and 23.4(1) Å, respectively.

FTIR spectra of samples are shown in Fig. 3.2. Various observed bands are assigned as follows [36, 45]. Broad bands centered around 3400 cm^{-1} are due to O-H stretching vibrations. Bands appearing around 1625 cm^{-1} are because of water molecule deformation vibrations. Sharp peaks at 1360 cm^{-1} are due to intercalated nitrate ions. Bands at about 663 cm^{-1} can be assigned to the δ(Co-O-H). Absorptions near 528 cm^{-1} are

---

This chapter is based on following published work:
Magnetic properties of undoped and Al doped layered α-Co(OH)$_2$, Anu Gupta and S. D. Tiwari, Physica B **525**, 21 (2017).

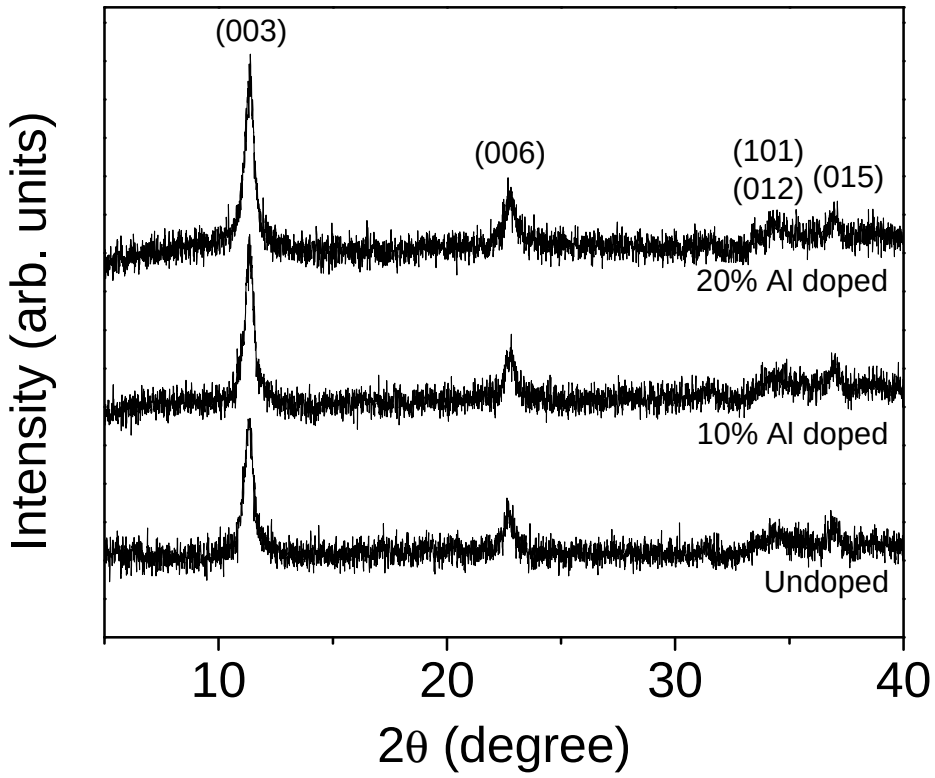

Fig. 3.1: Room temperature x-ray diffraction patterns of undoped, 10 and 20% Al doped α cobalt hydroxide.

due to Co-O stretching vibrations. This analysis yields the chemical formula of samples as $Co_{1-x}Al_x(OH)_{2-y+x}(NO_3)_y{\cdot}nH_2O$.

To determine values of parameters y and n, thermogravimetric analysis of all samples are performed. In this analysis, mass of a sample is recorded as a function of temperature as the sample is heated in air at a constant heating rate of 5 ^{0}C min^{-1}. Results of thermogravimetric analysis are shown in Fig. 3.3. First step of mass loss near 100 ^{0}C is due to loss of water. Second step near 200 ^{0}C is due to burning of intercalated nitrate and hydroxyl ions while converting the system to $CoO{\cdot}Co_{2-3x}Al_{3x}O_3$. Mass of each sample at 150 and 350 ^{0}C is used to determine values of n and y. This analysis yields the chemical formula of undoped, 10 and 20% Al

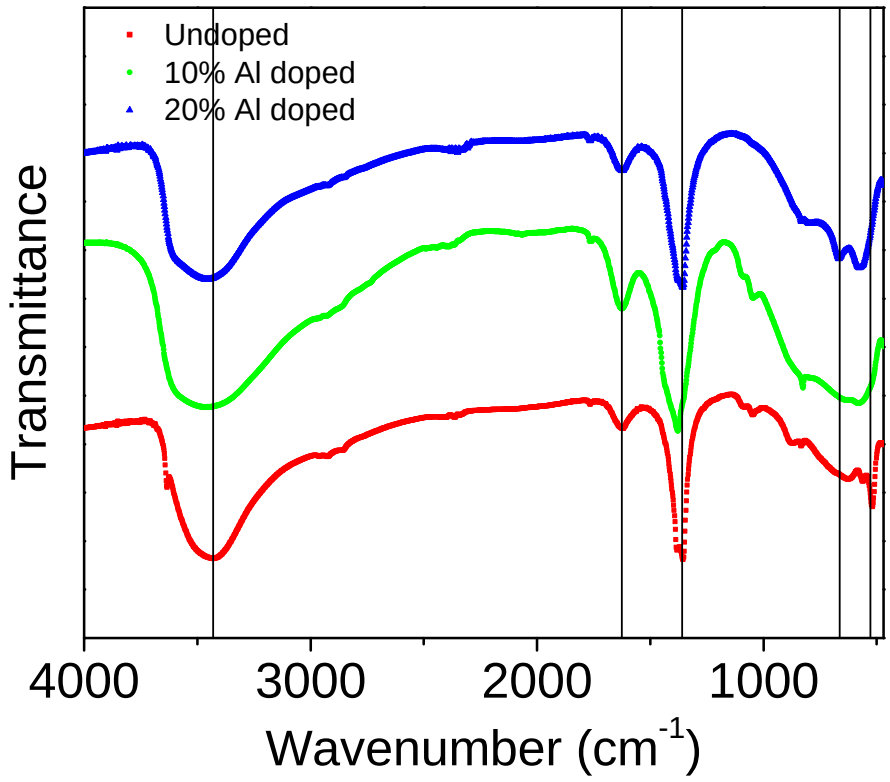

Fig. 3.2: FTIR spectra of undoped, 10 and 20% Al doped α cobalt hydroxide at room temperature. Curves are displaced in vertical direction arbitrarily.

doped samples as $Co(OH)_{1.84}(NO_3)_{0.16}{\cdot}0.69H_2O$, $Co_{0.9}Al_{0.1}(OH)_{1.87}(NO_3)_{0.23}{\cdot}0.61H_2O$ and $Co_{0.8}Al_{0.2}(OH)_{1.94}(NO_3)_{0.26}{\cdot}0.60H_2O$ respectively. Samples are also heated in air at 600 ^{0}C for three hours. Room temperature x-ray diffraction patterns of heated samples indicate the decomposition to spinel $CoO{\cdot}Co_{2-3x}Al_{3x}O_3$. A third step in mass loss at 850 ^{0}C is also observed in undoped sample only. This is due to reversible conversion of $CoO{\cdot}Co_2O_3$ to CoO [46]. This conversion is not observed in doped samples because the presence of trivalent Al^{3+} ions in the lattice hinders the process.

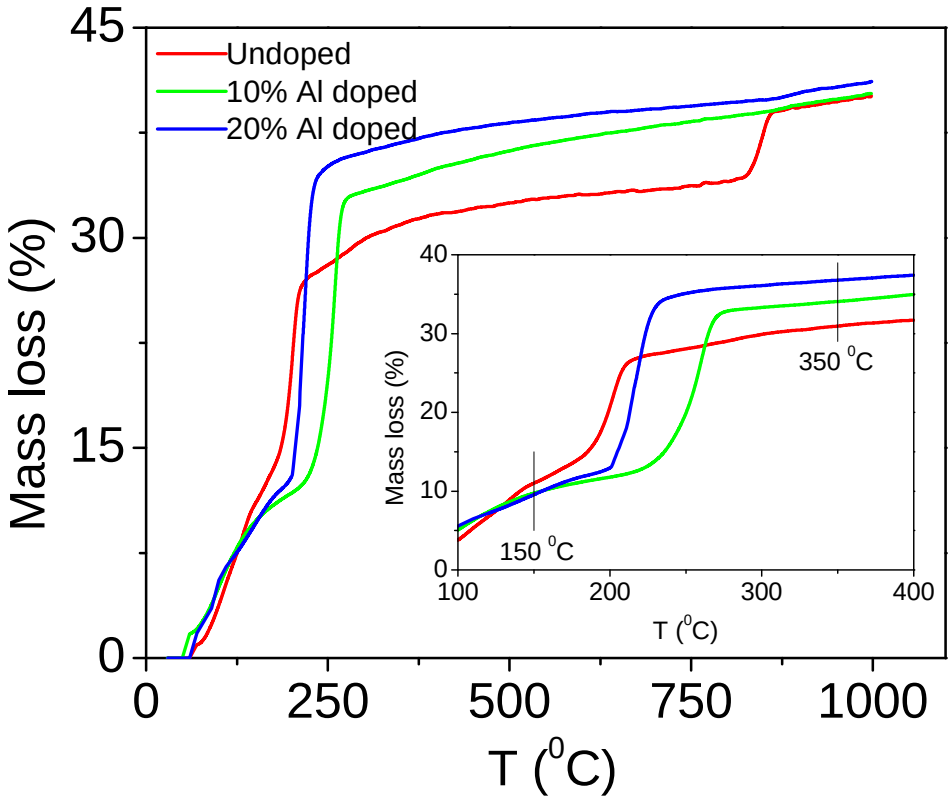

Fig. 3.3: Mass loss as a function of temperature for undoped, 10 and 20% Al doped α cobalt hydroxide. Inset shows magnified view of data in selected temperature range.

3.2 Magnetization

3.2.1 Temperature dependence

ZFC and FC susceptibility χ vs. temperature T data are measured in presence of 500 G magnetic field for undoped α cobalt hydroxide. The data are shown in Fig. 3.4. ZFC and FC susceptibility decrease with increasing temperature following same path. Inset (a) shows χ vs. T data at lower temperatures in presence of different applied magnetic fields. The 250 G data is seen to bifurcate at $T_{bf} = 7(1)$ K. This bifurcation of ZFC and FC curves disappears in higher magnetic fields. These are characteristics of superparamagnetic systems. The bifurcation temperature T_{bf} represents the beginning

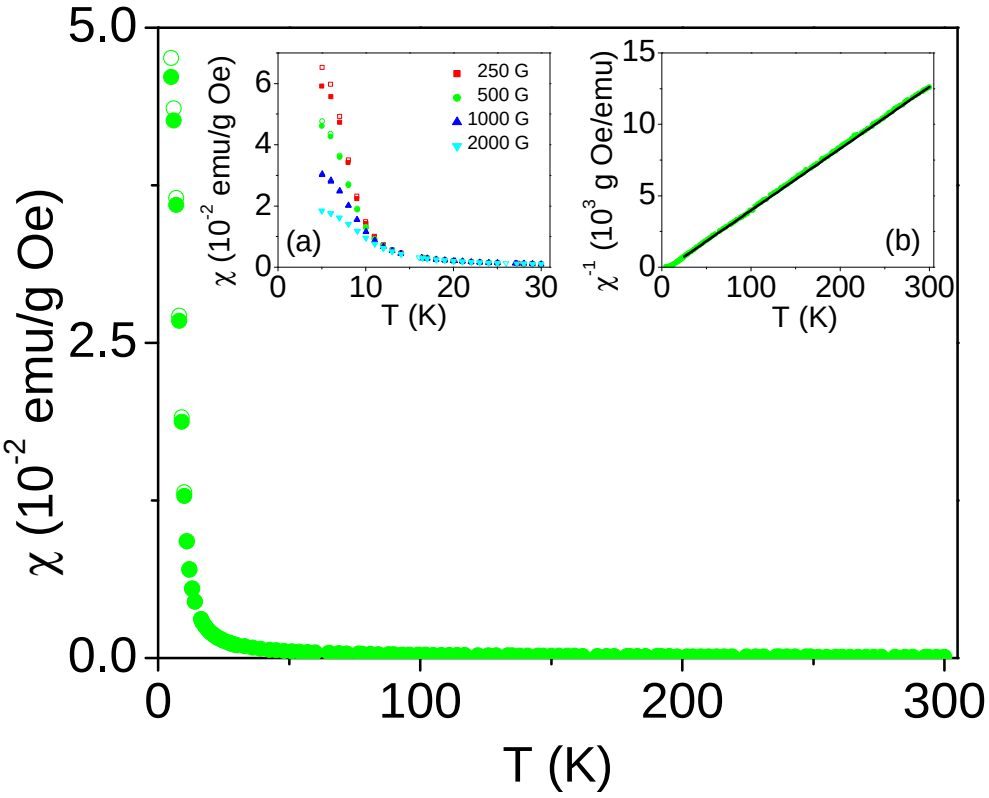

Fig. 3.4: ZFC (solid symbol) and FC (open symbol) susceptibility χ as a function of temperature T for undoped α cobalt hydroxide in 500 G applied magnetic field. Inset (a) shows magnified view of data at lower temperatures in different applied magnetic fields and (b) shows plot of χ^{-1} as a function of temperature. Solid line shows fit to Curie-Weiss law.

of blocking of particle magnetic moments. Inset (b) shows plot of inverse susceptibility vs. temperature for undoped α cobalt hydroxide. At higher temperature the plot looks to be linear. This linear portion of data is fitted to the Curie-Weiss law $\chi = \frac{C}{T-\theta}$. Values of fit parameters C and θ are estimated to be 0.02311 emu K/g Oe and 8.14 K respectively. The positive value of parameter θ indicates that the interaction among Co^{2+} ions in the system is ferromagnetic in nature. In Curie-Weiss law, value of parameter C is equal to $\frac{N\mu^2}{3k_B}$. Here N and k_B are number of Co^{2+} ions per unit mass and Boltzmann constant respectively. The value of ionic magnetic moment turns out to

be 4.56 μ_B. We should note that the estimated value of parameter θ does not represent actual Curie temperature of a system if more than one type of magnetic interactions are present [35].

From Curie-Weiss law one gets [35]

$$\frac{d(\chi T)}{dT} = -\frac{C\theta}{(T-\theta)^2}. \tag{3.1}$$

If one plots $\frac{d(\chi T)}{dT}$ as a function of temperature T then one should obtain a negative minimum at Curie temperature for a ferromagnetic transition and a positive maximum at Néel temperature for an antiferromagnetic transition. Figure 3.5(a) shows a plot of χT vs. temperature T for undoped α cobalt hydroxide in different applied magnetic fields whereas plots of $\frac{d(\chi T)}{dT}$ vs. temperature T in different applied magnetic fields are shown in Fig. 3.5(b). In this plot a negative minimum at $T_C = 9(1)$ K is seen. That is, the undoped α cobalt hydroxide undergoes a paramagnetic to ferromagnetic transition at 9(1) K. This transition temperature is also seen to be independent of applied magnetic field strength.

There should be two types of exchange interactions among Co^{2+} ions in α cobalt hydroxide. First one is strong ferromagnetic interaction in the hexagonal layer and second one is a weak ferromagnetic interaction between adjacent hexagonal layers [36]. In this way the system is overall a ferromagnet. Magnetic susceptibility χ of Co^{2+} ions in these layers can be described by a two dimensional Ising triangular lattice model [36, 47]

$$\chi = \frac{N\mu^2}{3k_BT}\sum_{n=0}^{8} a_n \left(\frac{2J_1}{k_BT}\right)^n, \tag{3.2}$$

where N is number of metal ions per unit mass. Here J_1 represents strength of exchange interaction among Co^{2+} ions in the hexagonal layers. The ZFC susceptibility as a function of temperature data in 500 G for undoped cobalt hydroxide, shown in Fig. 3.4,

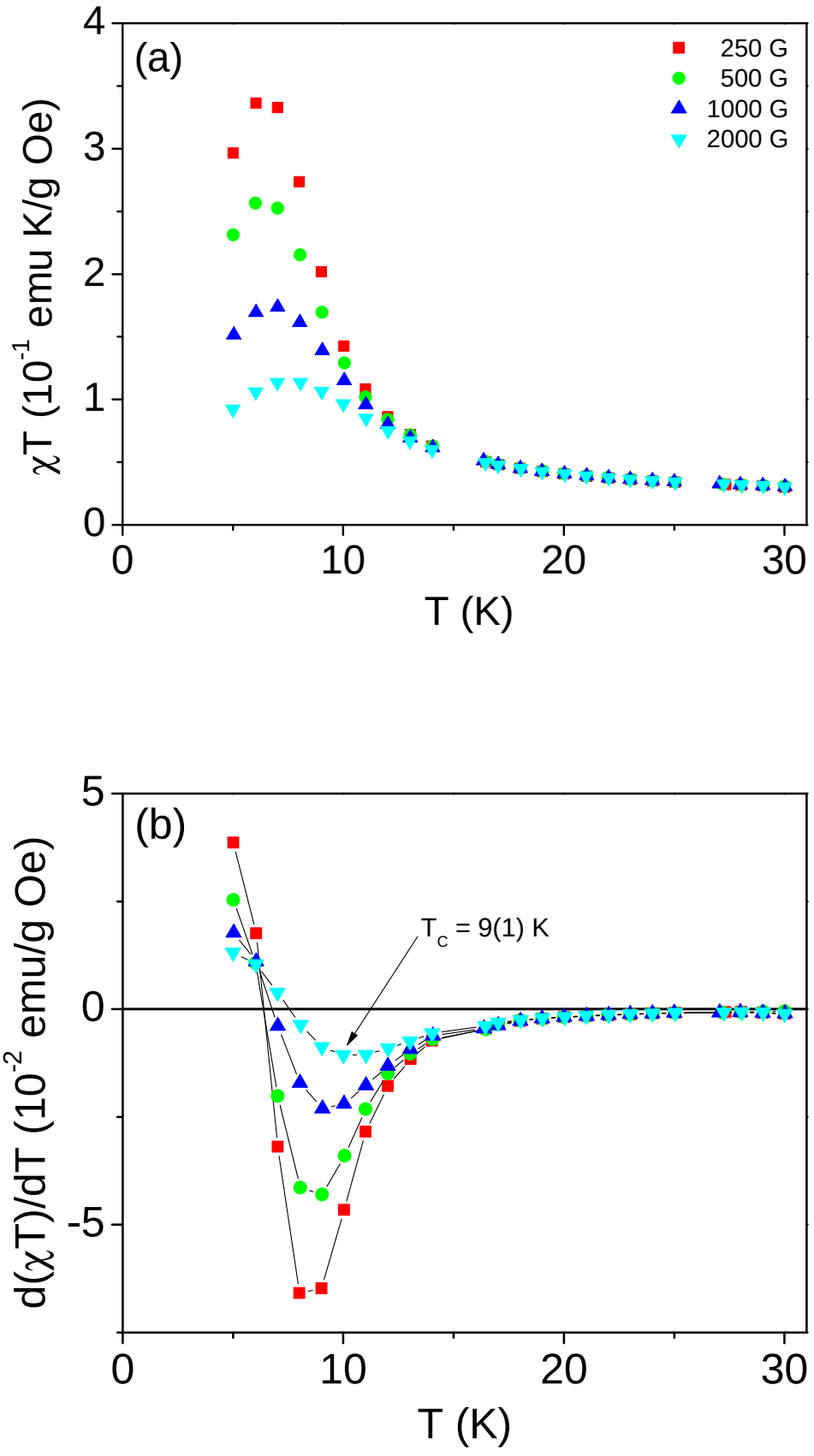

Fig. 3.5: (a) χT as a function of temperature in different applied magnetic fields and (b) $\frac{d(\chi T)}{dT}$ as a function of temperature for α cobalt hydroxide.

above 25 K are fitted to Eq. (3.2). Values of constants a_n are taken from elsewhere [36]. The data along with the fit are shown in Fig. 3.9. Values of resulting fit parameters μ and J_1 are shown in Table 3.1. Strength of interlayer exchange interaction J_2 can be estimated using relation [36, 48]

$$T_C = \frac{4\pi J_1}{ln(J_1/J_2)}, \tag{3.3}$$

where T_C is the Curie transition temperature. Table 3.1 also shows calculated value of J_2.

3.2.2 Field dependence

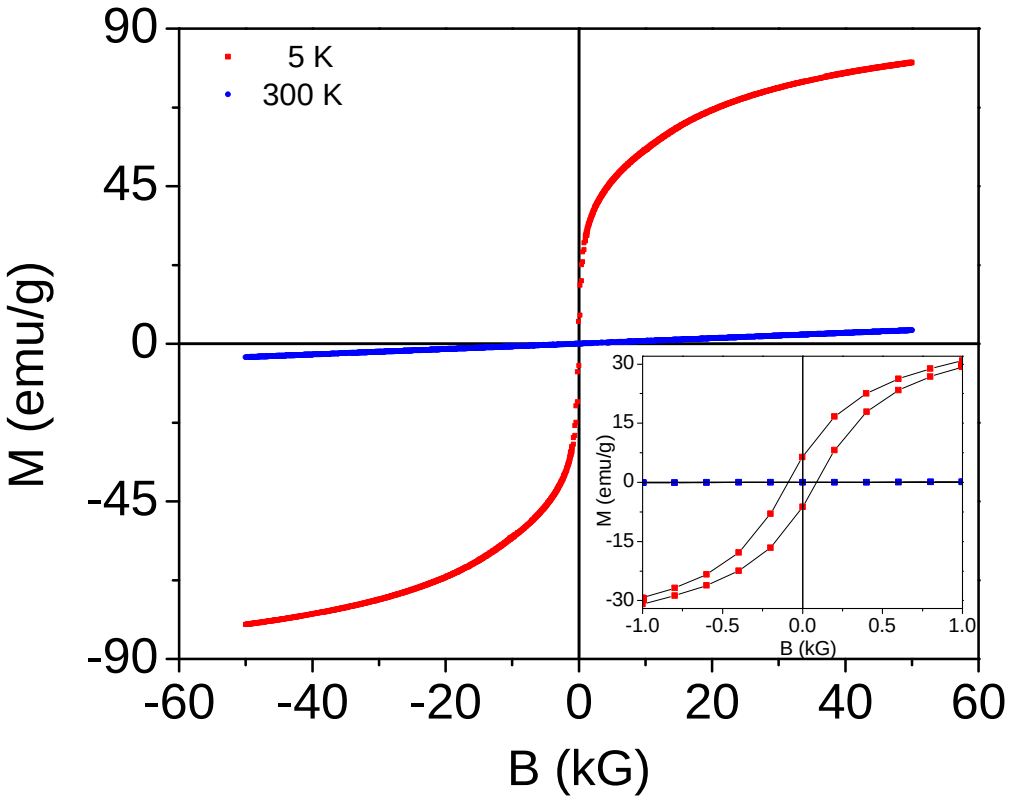

Fig. 3.6: M-B loops for undoped α cobalt hydroxide at 5 and 300 K. Inset shows a magnified view of data at lower fields.

Magnetization of undoped α cobalt hydroxide as a function of applied magnetic field is also measured. The data are shown in Fig. 3.6. The inset shows magnified view of data at lower magnetic fields. At 300 K, the magnetization of system changes linearly with applied magnetic field without any hysteresis because of system being in paramagnetic state. To see the behavior of system in ferromagnetic state, M-B loop at 5 K is also measured. A hysteresis in the curve at lower magnetic fields is clearly seen. The magnetization increases with increasing applied magnetic field strength. The same also has a tendency of saturation in higher magnetic fields. Saturation magnetization M_S of a ferromagnet in limit $T \to 0$ and $B \to \infty$ is given by $M_S = NgS\mu_B$. According to Hund rules, the value of spin quantum number S for Co^{2+} ion is $\frac{3}{2}$. In a recent work on β cobalt hydroxide, ground state of Co^{2+} ions is justified to have $S = \frac{1}{2}$ [49]. For undoped α cobalt hydroxide, using $g = 5.27$ and $S = \frac{1}{2}$, calculated $M_S \approx 131$ emu/g. From this value and Fig. 3.6, one finds that the magnetization is still far from saturation as it is measured at $T = 5$ K in maximum applied field of 50 kG.

3.2.3 Effect of Al doping

Magnetization of 10 and 20% Al doped samples of α cobalt hydroxide is also measured. The data are shown in Figs. 3.7 and 3.8. From these figures one sees that ZFC and FC susceptibility decrease with increasing temperature. The value of susceptibility decreases with increasing concentration of dopant. Values of parameters C and θ in Curie-Weiss law are estimated to be 0.02158 emu K/g Oe and 8.03 K respectively for 10% Al doped sample whereas for 20% Al doped sample values are 0.02032 emu K/g Oe and 7.94 K respectively. From inset (a) both samples are found to undergo paramagnetic to ferromagnetic transition. This transition temperature decreases with increasing amount of dopant. The M vs. B loop in inset (b) confirms paramagnetic nature at 300 K and ferromagnetic nature at 5 K. Hysteresis in the loops at 5 K at lower magnetic fields is also observed. These loops are not visible in the plots.

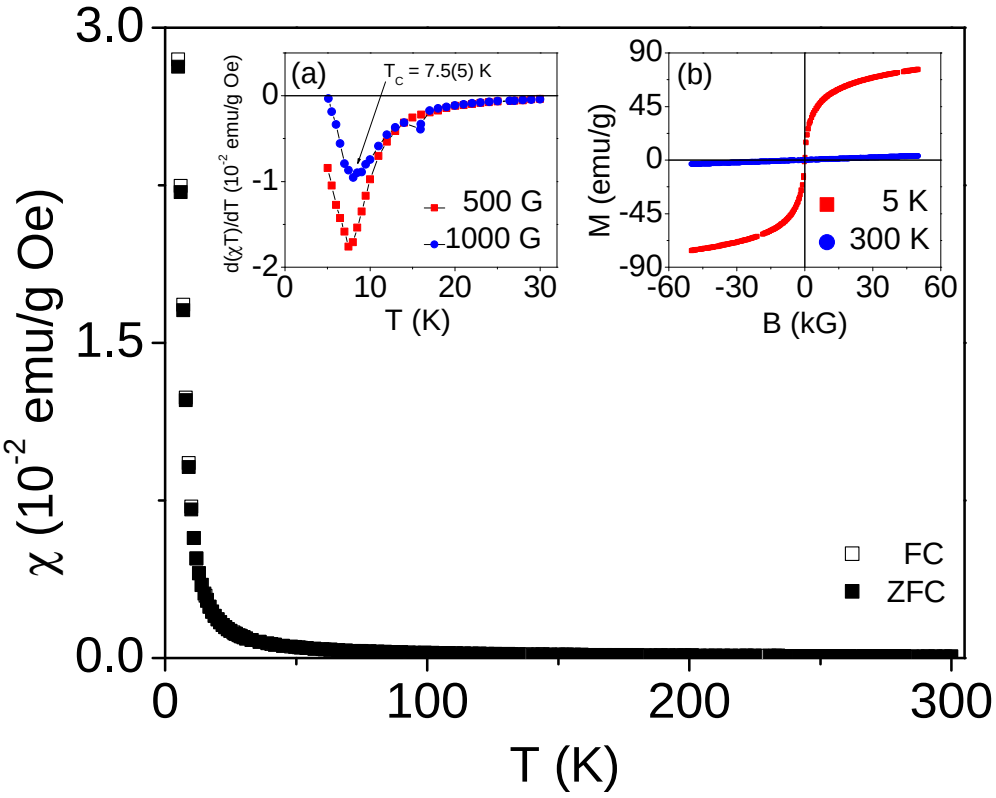

Fig. 3.7: ZFC (solid symbol) and FC (open symbol) susceptibility χ as a function of temperature T for 10% Al doped α cobalt hydroxide. Inset (a) shows $\frac{d(\chi T)}{dT}$ as a function of temperature T and (b) shows M-B loops at 5 and 300 K.

The magnetization of samples is seen to decrease with increasing concentration of non-magnetic Al^{3+} ions in the system. Because of the doping, the saturation magnetization of system and so average value of ionic magnetic moment μ must decrease as also evident from Table 3.1. Magnetic field of 50 kG at 5 K is not found to be sufficient to saturate the system. In fact, such systems require much higher magnetic fields at further lower temperatures to achieve saturation [36].

The ZFC susceptibility as a function of temperature data on Al doped α cobalt hydroxide are fitted to Eq. (3.2). The resulting fits along with the data are shown in Fig. 3.9. Estimated values of parameters μ and J_1 are shown in Table 3.1. This

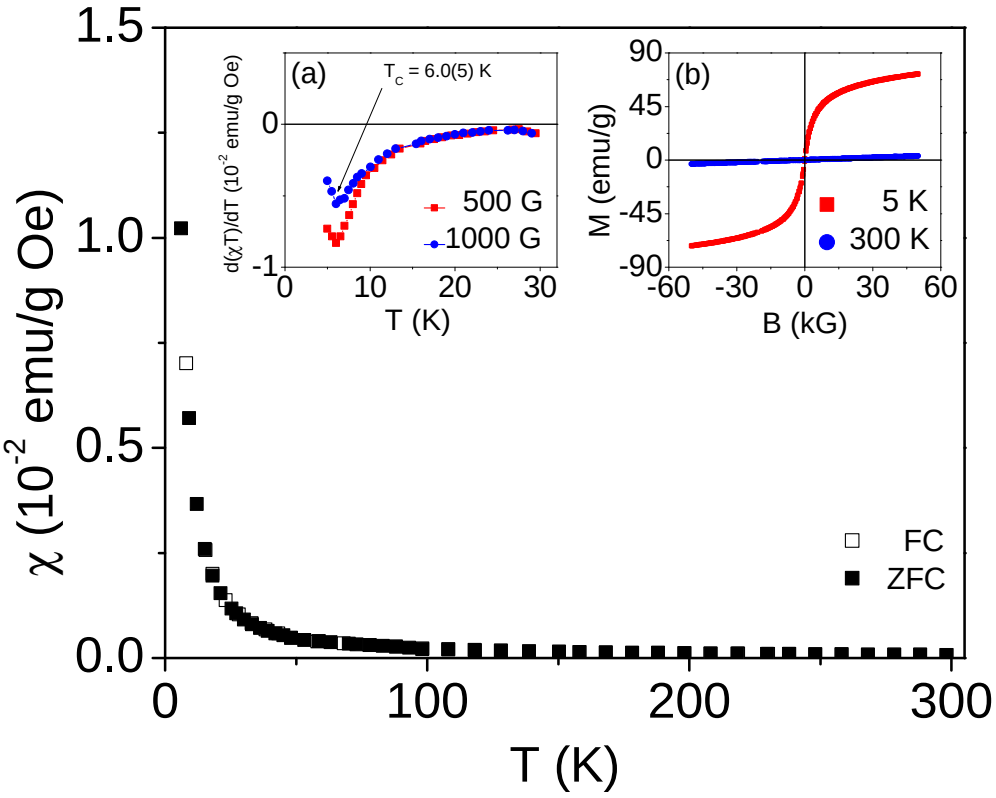

Fig. 3.8: ZFC (solid symbol) and FC (open symbol) susceptibility χ as a function of temperature T for 20% Al doped α cobalt hydroxide. Inset (a) shows $\frac{d(\chi T)}{dT}$ as a function of temperature T and (b) shows M-B loops at 5 and 300 K.

table also shows calculated values of J_2, g and M_S for samples. The Curie transition temperature T_C and so also exchange constants J_1 and J_2 are seen to decrease with increasing concentration of dopant.

Tab. 3.1: Estimated values of molecular weight (MW), Curie transition temperature T_C, average ionic moment μ, intralayer exchange interaction J_1, interlayer exchange interaction J_2, g factor and saturation magnetization M_S for undoped and Al doped α cobalt hydroxide.

Sample	MW (g mol^{-1})	T_C (K)	μ (μ_B)	J_1 (K)	J_2 (K)	g	Cal. M_S (emu/g)
Undoped	112.55	9(1)	4.56	1.070	0.240	5.27	131
10% Al doped	112.77	7.5(5)	4.40	1.059	0.180	5.08	126
20% Al doped	112.44	6.0(5)	4.26	1.048	0.117	4.92	122

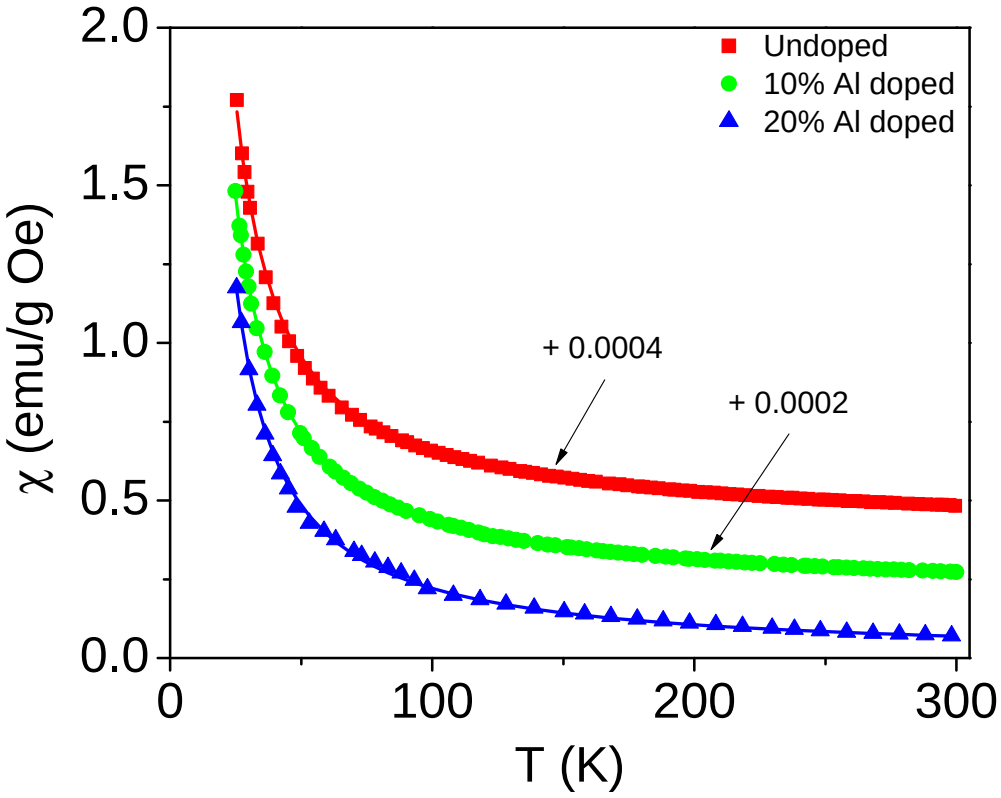

Fig. 3.9: ZFC susceptibility χ as a function of temperature T for undoped, 10 and 20% Al doped α cobalt hydroxide. Solid lines show fits to Eq. (3.2).

3.3 Conclusion

In this Chapter, detailed investigations on synthesis, structural characterization and magnetic behavior of undoped, 10 and 20% Al doped samples of alpha cobalt hydroxide nanoparticles are reported. All samples are found to undergo ferromagnetic transitions at lower temperatures. The corresponding Curie transition temperatures are seen to decrease with increasing concentration of Al in the lattice.

Chapter 4

BETA COBALT HYDROXIDE NANOPARTICLES

In this chapter structural, thermal and magnetic characterization of beta phase of cobalt hydroxide nanoparticles are discussed.

4.1 Structural Characterization

Room temperature XRD patterns of synthesized sample is shown in Fig. 4.1. The pattern confirms the formation of single phase β cobalt hydroxide [32]. Broadening in the peak indicates for nanocrystalline nature of sample. Average crystallite size, using Scherrer formula, comes out to be about 20 nm. Values of lattice parameters a and c of hexagonal unit cell are estimated to be 3.18(1) and 4.7(1) $\mathring{A}$ respectively. Almost similar values for lattice parameters are also reported by others [50].

FTIR spectra of the sample is shown in Fig. 4.2. Various observed bands are assigned as follows [35]. The sharp 3630 cm^{-1} band is assigned to free ν_{O-H} stretching in the OH group, broad band centered around 3430 cm^{-1} is due to absorbed water, the 1630 cm^{-1} band is due to δ_{H_2O} bending from absorbed water, 1385 cm^{-1} is due to Co-O stretching, 584 cm^{-1} band is due to δ_{O-H} bending in the O-H group and 490 cm^{-1}

This chapter is based on following published work:
Nature of magnetic interactions in β-Co(OH)$_2$ nanoparticles, Anu Gupta, S. D. Tiwari and Devendra Kumar, Physica Status Solidi B **253**, 1795 (2016).

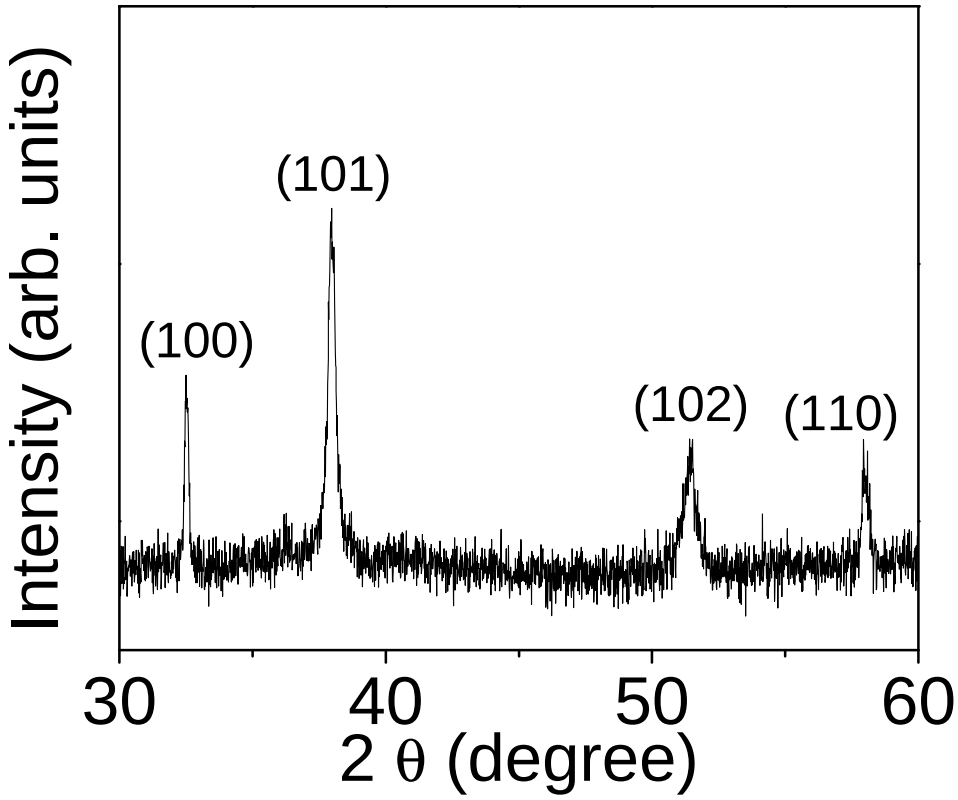

Fig. 4.1: Room temperature x-ray diffraction pattern of β cobalt hydroxide nanoparticles.

band is due to Co-O bending. This analysis yields the chemical formula of the sample as $Co(OH)_2 \cdot nH_2O$.

The sample is also characterized with thermogravimetric analyzer to estimate value of n. In this analysis, mass of the sample is measured while being heated in air at a constant rate. Figure 4.3 shows TGA curve for synthesized β cobalt hydroxide nanoparticles. It decomposes to Co_3O_4 on heating in air. In this decomposition, our sample undergoes a mass loss of 16.36%. A mass loss of 17.02% is also reported by others for cobalt hydroxide sample synthesized by similar method [46]. With the help of this analysis, value of n turns out to be 0.5. Mass loss above 800 ^{0}C is due to reversible conversion of $CoO \cdot Co_2O_3$ to CoO [46].

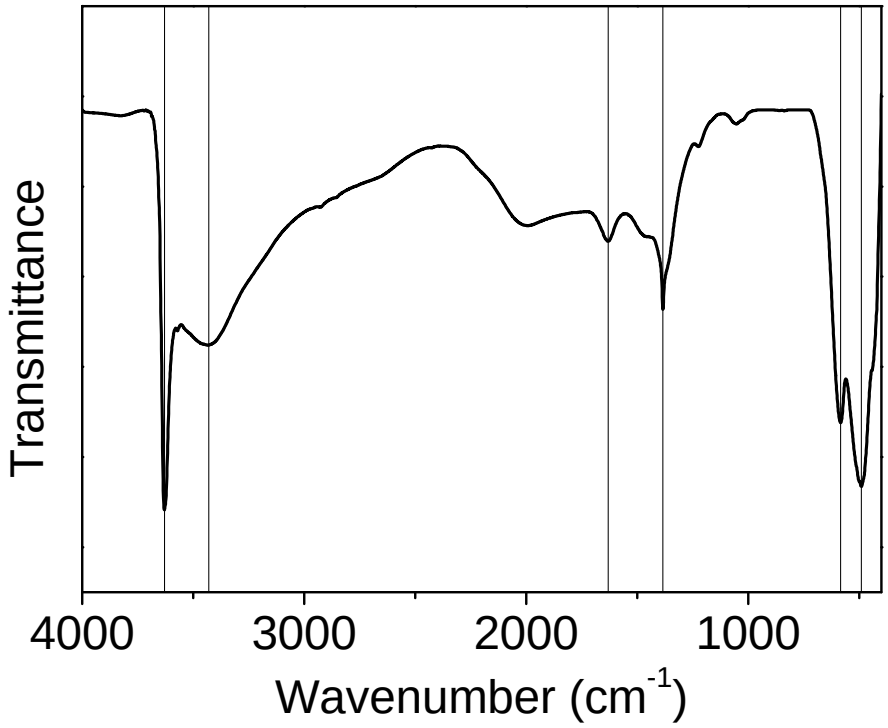

Fig. 4.2: FTIR spectra of β cobalt hydroxide at room temperature.

4.2 Magnetization

4.2.1 Temperature dependence

Figure 4.4 shows ZFC and FC susceptibility χ versus temperature T for the β cobalt hydroxide nanoparticles in presence of 500 G applied magnetic field. Both ZFC and FC susceptibility decrease with increasing temperature following the same path at higher temperatures. However, both curves are seen to bifurcate at lower temperature. Inset (a) shows magnified view of ZFC and FC data in different applied magnetic fields. Curves are always seen to bifurcate at 11(1) K. That is, the bifurcation temperature T_{bf} is found to be independent of the strength of applied magnetic field and so the behavior of present system is not superparamagnetic. In fact, this temperature represents the Néel transition temperature of the system. This issue will be discussed once again

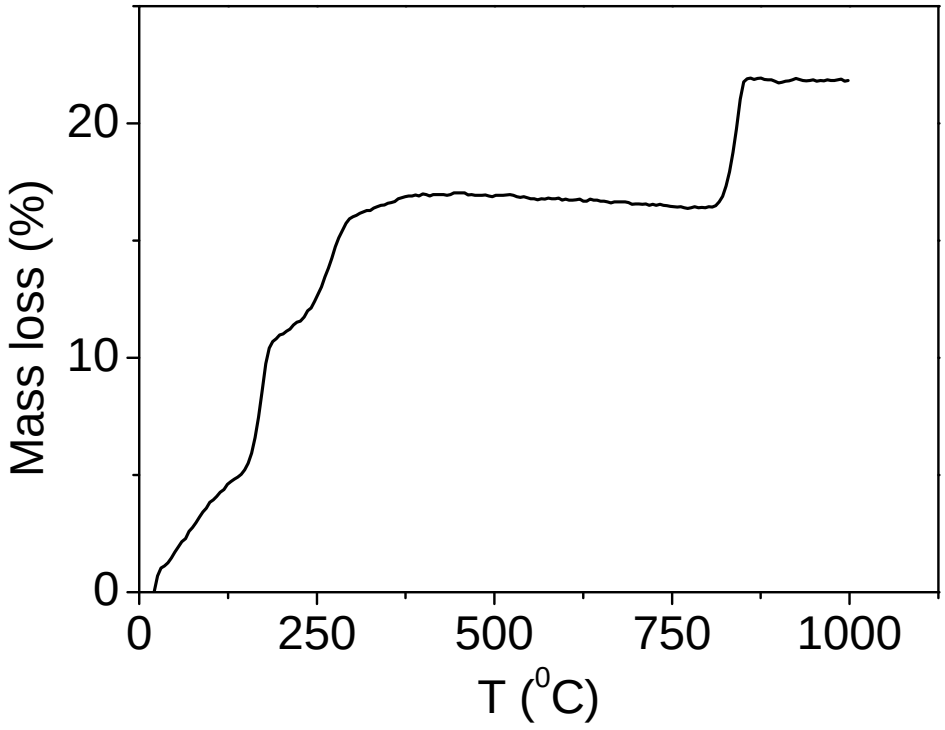

Fig. 4.3: Mass loss as a function of temperature for β cobalt hydroxide.

later. Low temperature specific heat capacity measurement also predicts the same value of Néel temperature for β cobalt hydroxide [34]. A peak in ZFC curve near to this temperature is also reported [28, 33, 51, 52]. Above a transition temperature θ, the magnetic susceptibility of ferro and antiferromagnetic materials is described by the Curie-Weiss law $\chi = \frac{C}{T-\theta}$. The parameter θ has a positive value for ferromagnetic interaction and has a negative value for antiferromagnetic interaction. In this way, one can characterize the nature of possible magnetic interaction in the system. Linear portion of χ^{-1} versus T curve should be fitted to a straight line to estimate values of parameters C and θ.

The crystal structure of β cobalt hydroxide is similar to that of β-$Ni(OH)_2$ [28, 29, 35]. In such compounds, three exchange interactions J_1, J_2 and J_3 are present [35]. Here J_1 represents strength of ferromagnetic exchange interaction among Co^{2+} ions lying in

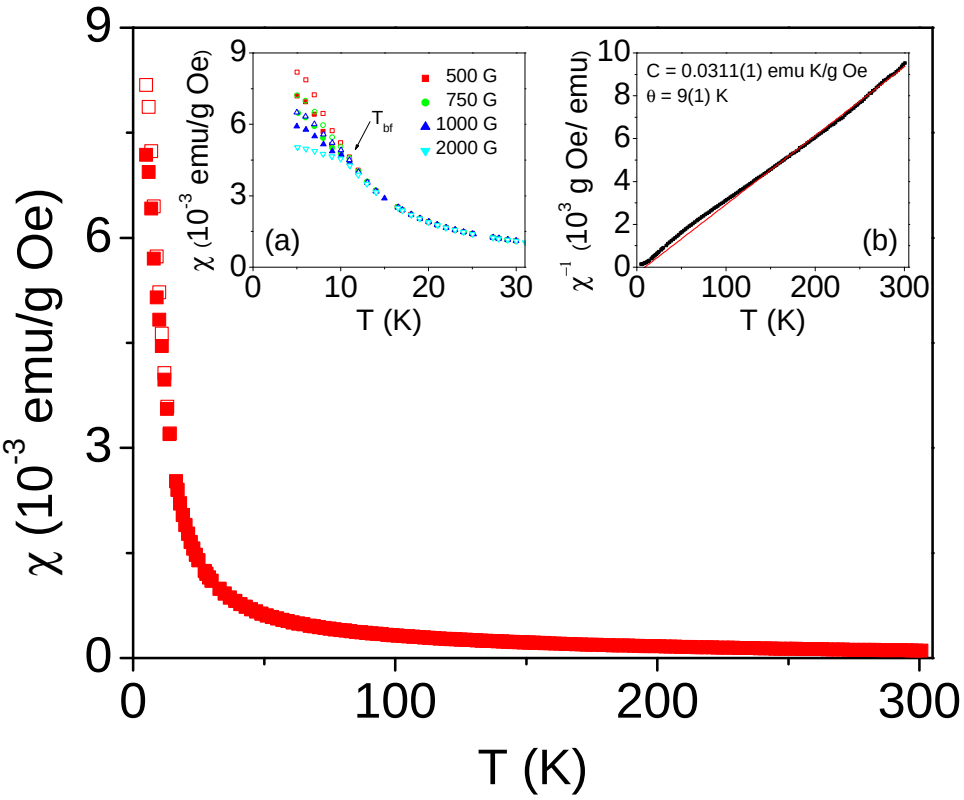

Fig. 4.4: Zero field cooled (solid symbol) and field cooled (open symbol) susceptibility χ as a function of temperature T for β cobalt hydroxide nanoparticles in 500 G applied magnetic field. Inset (a) shows magnified view of data at lower temperatures in different applied magnetic fields. Inset (b) shows plot of χ^{-1} as a function of temperature in 500 G applied magnetic field.

hexagonal layers, whereas J_2 and J_3 represent strength of possible antiferromagnetic interactions among Co^{2+} ions lying in neighboring hexagonal layers. Inset (b) in Fig. 4.4 shows a plot of inverse susceptibility versus temperature. Linear portion of this plot is fitted to a straight line. This fit is shown as a solid line. From this fit, values of parameters C and θ are estimated to be 0.0311(1) emu K/g Oe and 9(1) K respectively.

The values of spin quantum number S, orbital angular momentum quantum number L and total angular momentum quantum number J for Co^{2+} ion are $\frac{3}{2}$, 3 and $\frac{9}{2}$ respectively [1]. Theoretical values for spin magnetic moment and total magnetic

moment for Co^{2+} ion turn out to be 3.87 and 6.63 μ_B. The actual magnetic moment of Co^{2+} ion will depend on extent of quenching of orbital angular momentum in the system. In Curie-Weiss law, the value of parameter C is $\frac{N\mu^2}{3k_B}$, where N and k_B are number of Co^{2+} ions per unit mass and the Boltzmann constant respectively. Using the estimated value of parameter C, the value of magnetic moment μ for Co^{2+} ions in our sample turns out to be 5.03 μ_B. Somewhat similar values for ionic magnetic moment are also reported by others [28, 32]. Different values of fit parameters θ, in range 14 to 20 K, are also reported in literature [28,34,52]. However value of θ is found to be 9(1) K for present sample. It is worth mentioning here that the parameter θ in Curie-Weiss law does not represent actual Curie temperature or Néel temperature of a system if more than one type of magnetic interactions are present [35].

From Curie-Weiss law one gets [35]

$$\frac{d(\chi T)}{dT} = -\frac{C\theta}{(T-\theta)^2}. \tag{4.1}$$

Clearly, in a plot of $\frac{d(\chi T)}{dT}$ versus temperature T one should obtain a negative minimum at Curie temperature for a ferromagnetic transition and a positive maximum at Néel temperature for an antiferromagnetic transition. Figure 4.5 (a) shows a plot of χT versus temperature T for β cobalt hydroxide nanoparticles in different applied magnetic fields. Figure 4.5 (b) shows a plot of $\frac{d(\chi T)}{dT}$ versus temperature T. In this plot one sees a negative minimum at $T_1 = 13(1)$ K and a positive maximum at $T_2 = 9(1)$ K. That is, the β cobalt hydroxide nanoparticles undergo a two dimensional ferromagnetic ordering at 13(1) K and a three dimensional antiferromagnetic ordering at 9(1) K. Variation of T_1 and T_2 with applied magnetic field B is shown as an inset in Fig. 4.5 (b). Both transition temperatures are seen to be independent of the strength of applied magnetic field.

In β cobalt hydroxide, the Co^{2+} spins in antiferromagnetic state are parallel to the

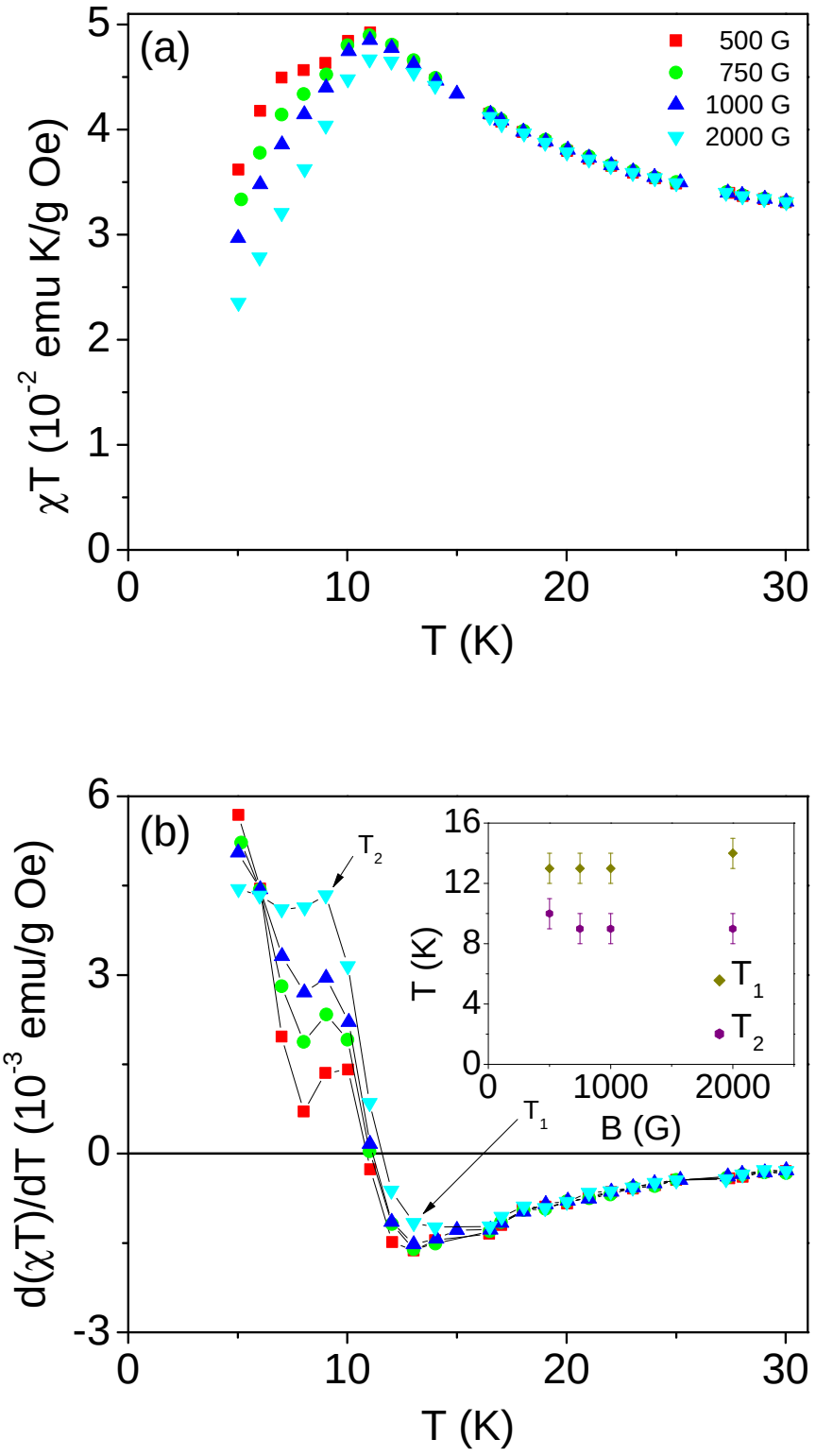

Fig. 4.5: (a) χT as a function of temperature T for β cobalt hydroxide nanoparticles in different applied magnetic fields. (b) $\frac{d(\chi T)}{dT}$ as a function of temperature T. Inset shows plot of T_1 and T_2 as a function of applied magnetic field B.

c-axis within each c plane with alternate c planes aligned antiferromagnetically [28]. The Hamiltonian of the system, considering the Ising model, is given by

$$\mathcal{H} = -2\sum_{i,j} J_{ij}\vec{S_i}\cdot\vec{S_j}. \tag{4.2}$$

Equations for θ and T_N are [35]

$$3k_B\theta = 2S(S+1)[J_1Z_1 + J_2Z_2 + J_3Z_3] \tag{4.3}$$

and

$$3k_BT_N = 2S(S+1)[J_1Z_1 - J_2Z_2 - J_3Z_3], \tag{4.4}$$

where k_B is the Boltzmann constant. Here $Z_1 = 6$, $Z_2 = 2$ and $Z_3 = 12$ are the appropriate number of neighbors involved in the exchange constants J_1, J_2 and J_3 respectively for the hexagonal lattice [35]. Also $J_2 = 3\ J_3$. For present system, $\theta =$ 9(1) K, T_N = 13(1) K (the temperature at which two dimensional ordering sets in) and $2S(S+1) = \frac{15}{2}$. From Eqs. (4.3) and (4.4) values of exchange constants J_1, J_2 and J_3 turn out to be about 0.73, -0.12 and -0.03 K respectively. The exchange constant J_1 has a positive value and exchange constants J_2 and J_3 have negative values. Also, the magnitude of J_1 is largest. These indicate that the intraplaner exchange interaction among Co^{2+} ions is ferromagnetic in nature and is stronger than two interplaner antiferromagnetic interactions.

4.2.2 Field dependence

Magnetization of β cobalt hydroxide nanoparticles versus applied magnetic field is also measured at 5 and 300 K. These measurements are shown in Fig. 4.6. This figure shows that the magnetization of system, at 300 K, increases linearly with increasing strength of applied magnetic field as per expectation in paramagnetic region. At 5 K,

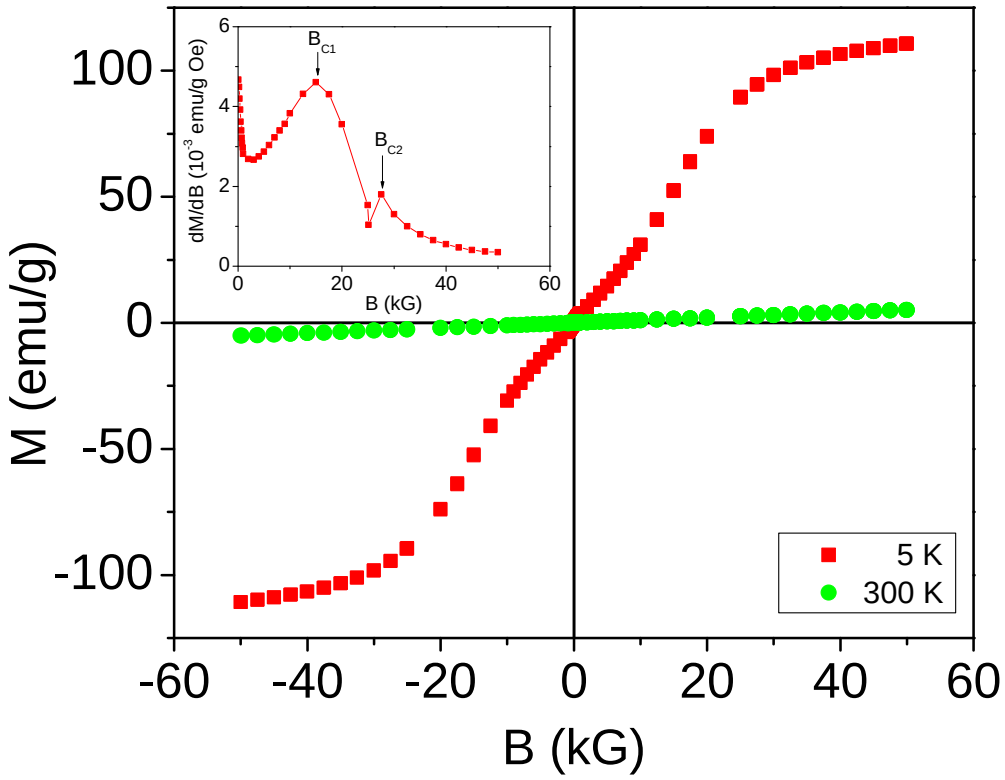

Fig. 4.6: M-B loops at 5 and 300 K for β cobalt hydroxide nanoparticles. Inset shows a plot of $\frac{dM}{dB}$ as a function of applied magnetic field B at 5 K.

the magnetization initially increases almost linearly with increasing strength of applied magnetic field followed by a sudden rise in the magnetization at higher magnetic fields. Inset in Fig. 4.6 shows a plot of $\frac{dM}{dB}$ versus applied magnetic field B. In this plot two peaks are seen at magnetic fields $B_{C1} \approx 15$ kG and $B_{C2} \approx 28$ kG. Similar behavior has also been observed for β-Ni(OH)$_2$ nanoparticles [35]. The peak at B_{C1} is attributed to the switching of spins lying on the surface of particles from antiparallel orientation to a direction parallel to the applied magnetic field. The system undergoes a magnetic field induced transition, also known as metamagnetism, from antiferromagnetic to ferromagnetic order at B_{C2}. This magnetic field induced transition is also evident from the behavior of M versus B curve at 5 K at higher magnetic fields. Also $B_{C2} \approx 2$

B_{C1}, as per expectation [35]. The saturation magnetization M_S of a ferromagnet near 0 K is given by $M_S = NgS\mu_B$. For present sample of β cobalt hydroxide particles, using $g = 2.60$ and $S = \frac{3}{2}$ yields the calculated $M_S = 214$ emu/g. From this value and Fig. 4.6, a magnetic field of 50 kG at 5 K is not found to be sufficient to saturate the system. In fact, such systems require magnetic field of few hundred kilogauss strength for saturation at low temperatures [35].

4.3 Conclusion

In this chapter, magnetic behavior of 20 nm β-$Co(OH)_2 \cdot 0.5H_2O$ particles is discussed. This system has three exchange interactions among Co^{2+} ions. The intraplaner exchange interaction is found to be ferromagnetic in nature. This interaction is seen to dominate over two weaker interplaner antiferromagnetic exchange interactions. The system is also found to undergo a magnetic field induced transition from antiferromagnetic to ferromagnetic state at low temperature.

Chapter 5

ALPHA NICKEL HYDROXIDE NANOPARTICLES

In this chapter synthesis, structural and magnetic characterization of undoped and Al doped α nickel hydroxide nanoparticles are presented.

5.1 Structural Characterization

Room temperature XRD patterns of undoped, 10 and 20% Al doped nickel hydroxide nanoparticles are shown in Fig. 5.1. The patterns confirm the formation of single phase α nickel hydroxide [36]. Broadening in the peaks indicates for nanocrystalline nature of samples. Average crystallite size, using Scherrer formula, comes out to be about 6 nm. Values of lattice parameters a and c of hexagonal unit cell are estimated to be 3.06(2) and 24.4(1) Å, respectively.

Fourier transform infrared spectra of the samples are shown in Fig. 5.2. Observed bands are assigned as follows [53]. Broad bands centered around 3500 cm^{-1} are due to O-H stretching vibrations. Bands appearing around 1625 cm^{-1} are because of water molecule deformation vibrations. Intense peaks at 1380 cm^{-1} are due to intercalated nitrate ions between hexagonal layers. Bands around 655 cm^{-1} are due to δ(Ni-O-H) and absorptions near 470 cm^{-1} are due to Ni-O stretching vibrations. This analysis provides the molecular formula of samples as $Ni_{1-x}Al_x(OH)_{2-y+x}(NO_3)_y \cdot nH_2O$.

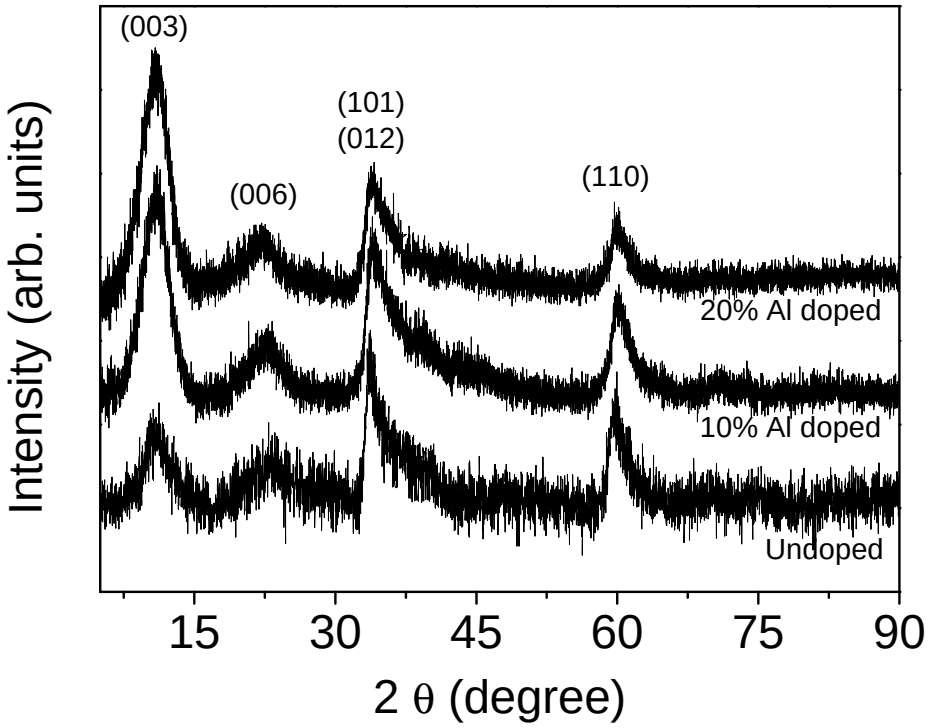

Fig. 5.1: Room temperature x-ray diffraction patterns of undoped, 10 and 20% Al doped α nickel hydroxide.

Thermogravimetric analysis of the samples are performed to determine values of parameters y and n. For this, the samples are heated in air at a constant heating rate of 5 ^{0}C min^{-1}. Results are shown in Fig. 5.3. Mass loss near 100 ^{0}C are due to loss of water. Mass loss near 200 ^{0}C are due to burning of intercalated nitrate and hydroxyl ions while converting the system to $Ni_{1-x}Al_xO_{1+\frac{x}{2}}$. Mass of samples at 200 and 550 ^{0}C are used to determine values of n and y. This analysis yields the molecular formula of undoped, 10 and 20% Al doped samples as $Ni(OH)_{1.87}(NO_3)_{0.13}{\cdot}0.94H_2O$, $Ni_{0.9}Al_{0.1}(OH)_{2.02}(NO_3)_{0.08}{\cdot}0.83H_2O$ and $Co_{0.8}Al_{0.2}(OH)_{2.10}(NO_3)_{0.10}{\cdot}0.74H_2O$ respectively. The samples are also heated in air at 700 ^{0}C for three hours. Room temperature x-ray diffraction patterns of heated samples indicate the decomposition of original samples to cubic $Ni_{1-x}Al_xO_{1+\frac{x}{2}}$.

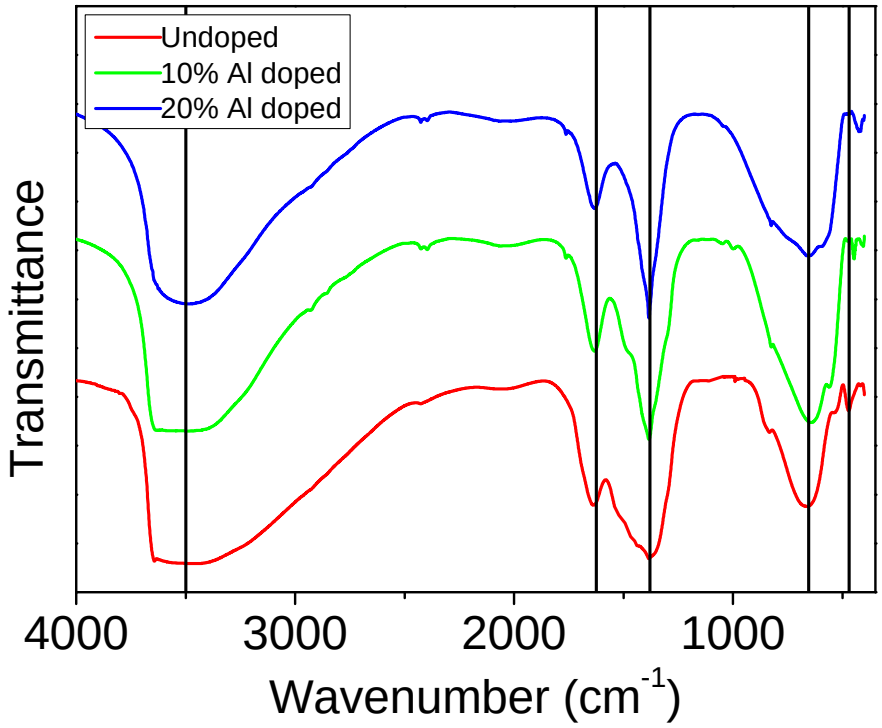

Fig. 5.2: FTIR spectra of undoped, 10 and 20% Al doped α nickel hydroxide. Curves are displaced in vertical direction arbitrarily.

5.2 Magnetization

5.2.1 Temperature dependence

Figure 5.4 shows zero field cooled (ZFC) and field cooled (FC) susceptibility χ versus temperature T in 500 G applied magnetic field for undoped α nickel hydroxide. The ZFC curve is seen to peak at 13(1) K. Both susceptibility decrease with increasing temperature above the peak temperature. The FC susceptibility is seen to decrease monotonically with increasing temperature. Inset (a) shows χ vs. T data in temperature range 5-30 K in presence of different applied magnetic fields. The 250 G data are seen to peak at 16 K. The peak temperature decreases with increasing strength of applied magnetic field. These are characteristic features of superparamagnetic systems. The peak temperature T_p is called the blocking temperature. Inset (b) shows a plot of

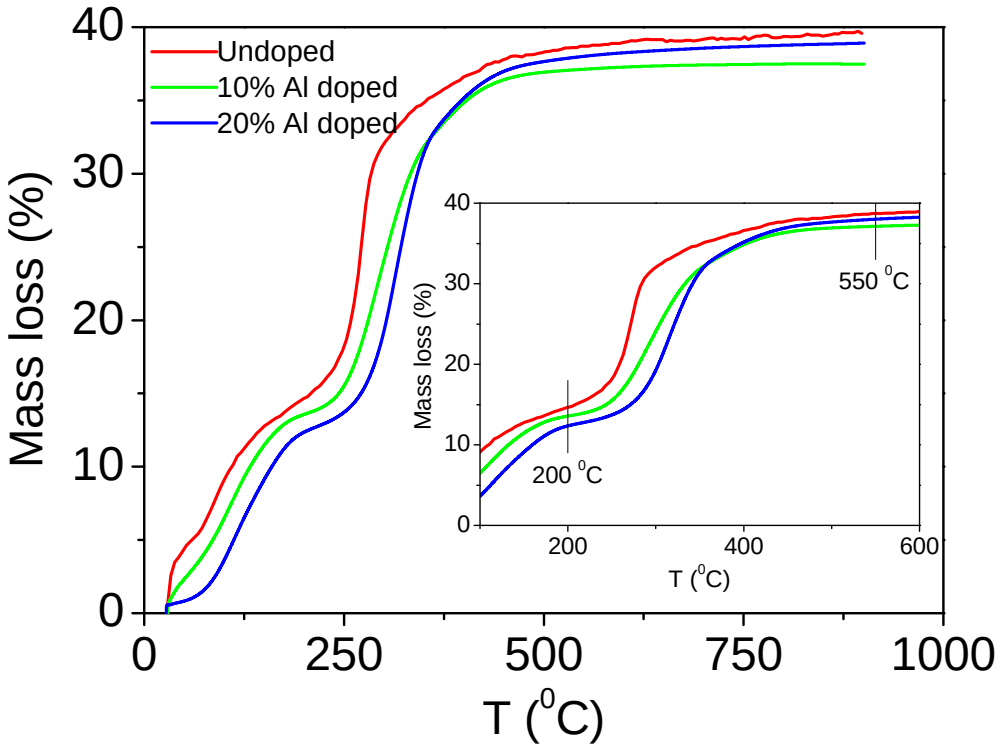

Fig. 5.3: Mass loss as a function of temperature for undoped, 10 and 20% Al doped α nickel hydroxide.

χ^{-1} versus temperature T for undoped α nickel hydroxide. The plot looks to be linear at higher temperatures. The linear portion of data is fitted to the Curie-Weiss law $\chi = \frac{C}{T-\theta}$. Values of fit parameters C and θ turn out to be 0.01443 emu K/g Oe and 20.6 K respectively. The positive value of parameter θ indicates that the interaction among Ni^{2+} ions in undoped α nickel hydroxide is ferromagnetic in nature. Value of parameter C equals to $\frac{N\mu^2}{3k_B}$, where N and k_B are number of metal ions per unit mass and Boltzmann constant respectively. Value of ionic magnetic moment μ turns out to be 3.65 μ_B. The value of parameter θ represents Curie temperature of a system only if one type of magnetic interaction is present [35]. There is also another way to estimate the Curie temperature of a system. Term χT represents magnetic energy and its temperature derivative is proportional to heat capacity of the system [54]. That

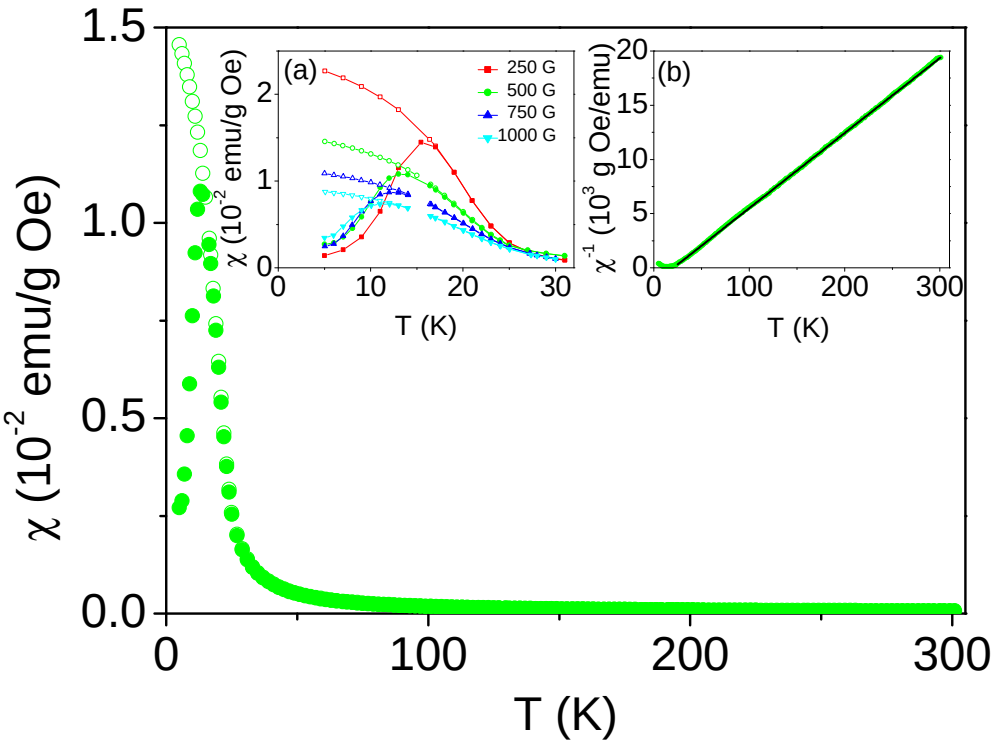

Fig. 5.4: ZFC (solid symbol) and FC (open symbol) susceptibility χ as a function of temperature T for undoped α nickel hydroxide in 500 G applied magnetic field. Inset (a) shows magnified view of data in low temperature range in different applied magnetic fields and (b) shows plot of χ^{-1} as a function of temperature. Fit to Curie-Weiss law is shown as solid line.

is, signature of any magnetic transition can easily be found in a plot of $\frac{d(\chi T)}{dT}$ versus temperature T. The Curie-Weiss law gives

$$\frac{d(\chi T)}{dT} = -\frac{C\theta}{(T-\theta)^2}. \tag{5.1}$$

Here θ being positive for ferromagnetic transition and negative for antiferromagnetic transition. Figure 5.5(a) shows a plot of χT versus temperature T and Fig. 5.5(b) shows plot of $\frac{d(\chi T)}{dT}$ versus temperature T for undoped α nickel hydroxide in different applied magnetic fields. The minimum in this plot at temperature $T_1 = 21(1)$ K represents ferromagnetic transition temperature for Ni^{2+} ions in (001) layers. This

transition temperature is seen to be independent of applied magnetic field strength. The transition at temperature T_2 does not represent any antiferromagnetic transition in the system as it has strong field dependence. Applied magnetic field dependence of peak temperature T_p in χ vs. T curves is also shown in inset of Fig. 5.5(b). Both T_2 and T_p are seen to have similar magnetic field dependence. Therefore, T_2 must represent blocking temperature for particle magnetic moments of undoped α nickel hydroxide particles. The blocking temperature is well known to decrease with increasing strength of applied magnetic field [55].

Due to large value of lattice parameter c in comparison to that of a, there exist two types of exchange interactions among Ni^{2+} ions present in the system. One is ferromagnetic exchange interaction in the hexagonal layer and another is ferromagnetic exchange interaction between adjacent hexagonal layers. The second interaction must be much weaker than first one because $c \gg a$. The system is overall a ferromagnet. The magnetic susceptibility χ of Ni^{2+} ions in these layers can be well described by a two dimensional Ising triangular lattice model [47]

$$\chi = \frac{N\mu^2}{3k_BT} \sum_{n=0}^{8} a_n \left(\frac{2J_1}{k_BT}\right)^n, \tag{5.2}$$

where N is number of metal ions per unit mass. Here J_1 represents strength of exchange interaction among Ni^{2+} ions in the hexagonal layers. Values of constants a_n are taken as such from elsewhere [36]. Considering only first term in the series gives Curie variation. The ZFC susceptibility versus temperature data in 500 G for undoped α nickel hydroxide above 25 K are fitted to Eq. (5.2). The data and fit are shown in Fig. 5.6. Estimated values of parameters μ and J_1 are shown in Table 5.1. The strength of interlayer exchange interaction J_2 can be estimated using relation [48]

$$T_C = \frac{4\pi J_1}{ln(J_1/J_2)}. \tag{5.3}$$

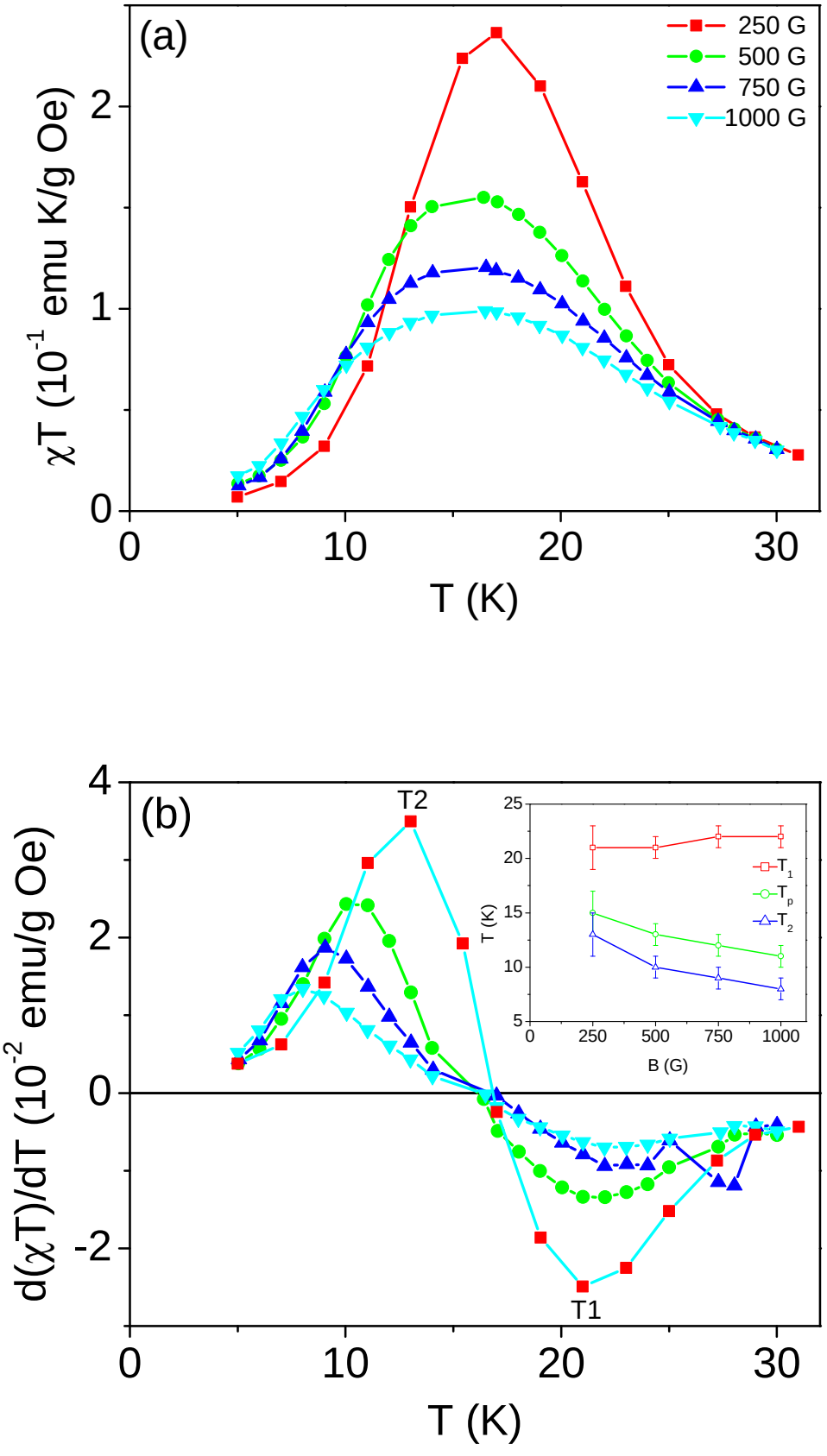

Fig. 5.5: (a) χT as a function of temperature in different applied magnetic fields and (b) $\frac{d(\chi T)}{dT}$ as a function of temperature for undoped α nickel hydroxide.

Here T_C is the Curie transition temperature. Estimated value of J_2 is shown in Table 5.1.

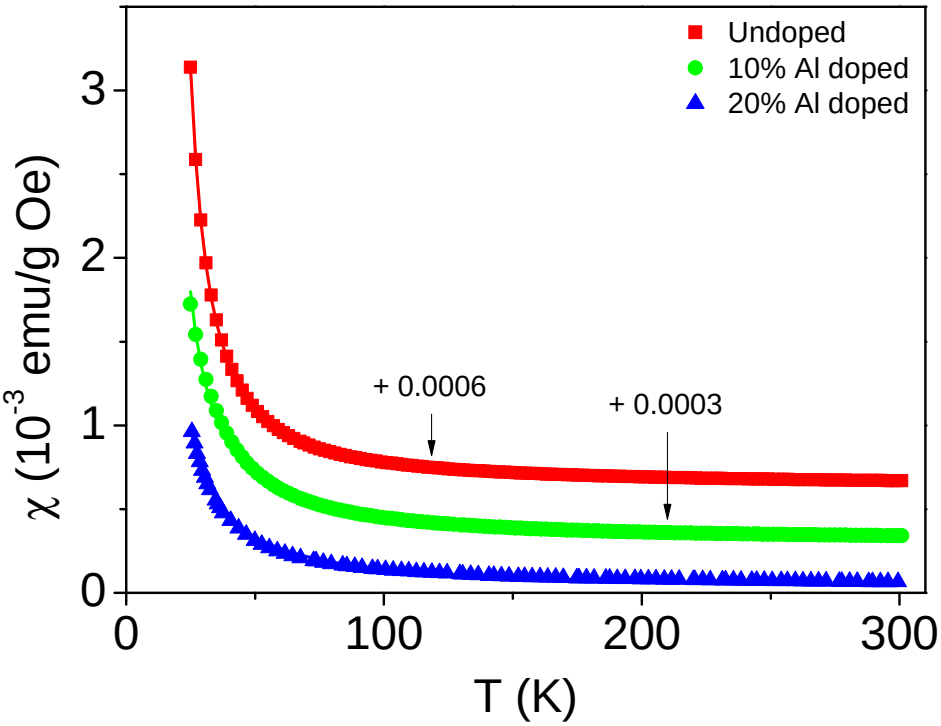

Fig. 5.6: ZFC susceptibility χ as a function of temperature T for undoped, 10 and 20% Al doped α nickel hydroxide. Solid lines show fits to Eq. (5.2).

5.2.2 Field dependence

Figure 5.7 shows M-B loops for undoped α nickel hydroxide at two different temperatures. At 300 K, the magnetization of system changes linearly with applied magnetic field without any hysteresis. This behavior is due to paramagnetic nature of the system at 300 K. On other hand at 5 K, magnetization increases with increasing applied magnetic field strength with a hysteresis at lower magnetic fields. Saturation magnetization M_S of a ferromagnetic material in limit $T \to 0$ and $B \to \infty$ is given by relation $M_S = NgS\mu_B$. For undoped α nickel hydroxide, using $g = 2.58$ and $S = 1$,

Tab. 5.1: Estimated values of molecular weight (MW), Curie transition temperature T_C, average ionic moment μ, intralayer exchange interaction J_1, interlayer exchange interaction J_2, g factor and saturation magnetization M_S for undoped and Al doped α nickel hydroxide.

Sample	MW (g mol^{-1})	T_C (K)	μ (μ_B)	J_1 (K)	J_2 (K)	g	M_S (emu/g)
Undoped	115.46	21(1)	3.65	2.894	0.512	2.58	125
10% Al doped	109.76	11(1)	3.44	2.266	0.170	2.43	124
20% Al doped	107.57	6(1)	3.24	1.705	0.048	2.29	119

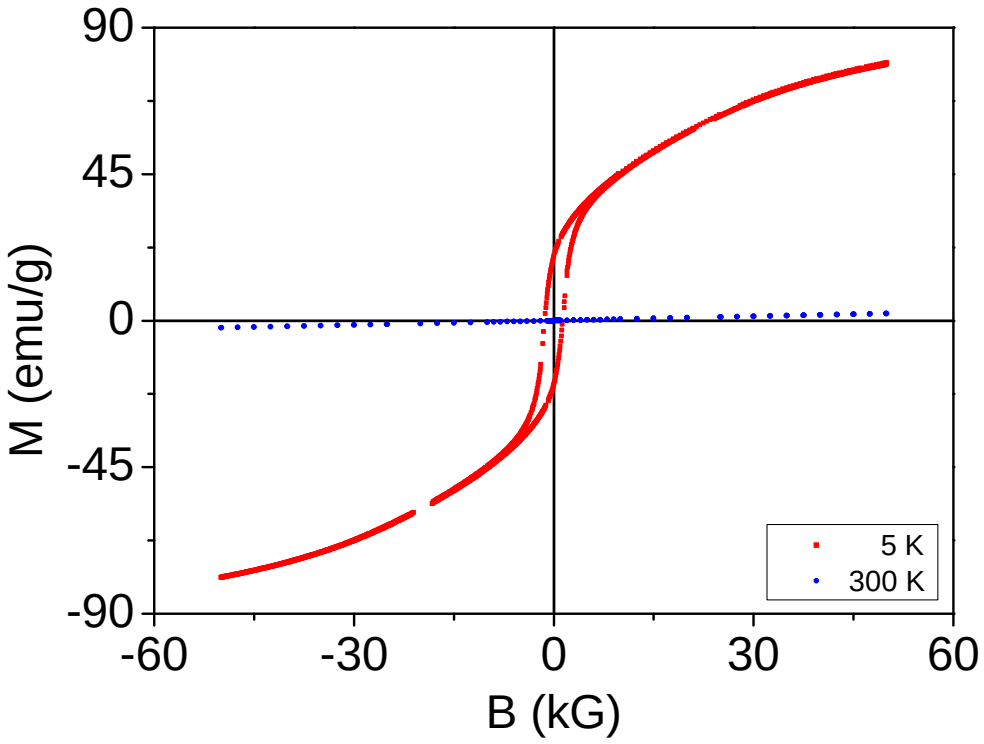

Fig. 5.7: M-B loops for undoped α nickel hydroxide at 5 and 300 K.

one gets calculated $M_S \approx 125$ emu/g. Clearly, from Fig. 5.7, the magnetization is still far from saturation as it is measured at $T = 5$ K in maximum applied field of 50 kG. Magnetization measurement at further lower temperature and much higher magnetic field is required to achieve saturation.

5.2.3 Effect of Al doping

In this work, magnetic behavior of 10 and 20% Al doped samples of α nickel hydroxide is also studied. The magnetization data on these samples are shown in Figs. 5.8 and 5.9. The ZFC and FC susceptibility decrease with increasing temperature monotonically following same path. Both samples undergo paramagnetic to ferromagnetic transition as evident from inset (a). The M-B loops in inset (b) confirm paramagnetic nature at 300 K and ferromagnetic nature at 5 K. The 5 K loops also have hysteresis, not visible in plots, at lower magnetic fields. The magnetization of samples is seen to decrease with increasing concentration of non-magnetic Al^{3+} ions in the system. Because of this doping, average ionic magnetic moment μ decreases. Molar mass of samples quite

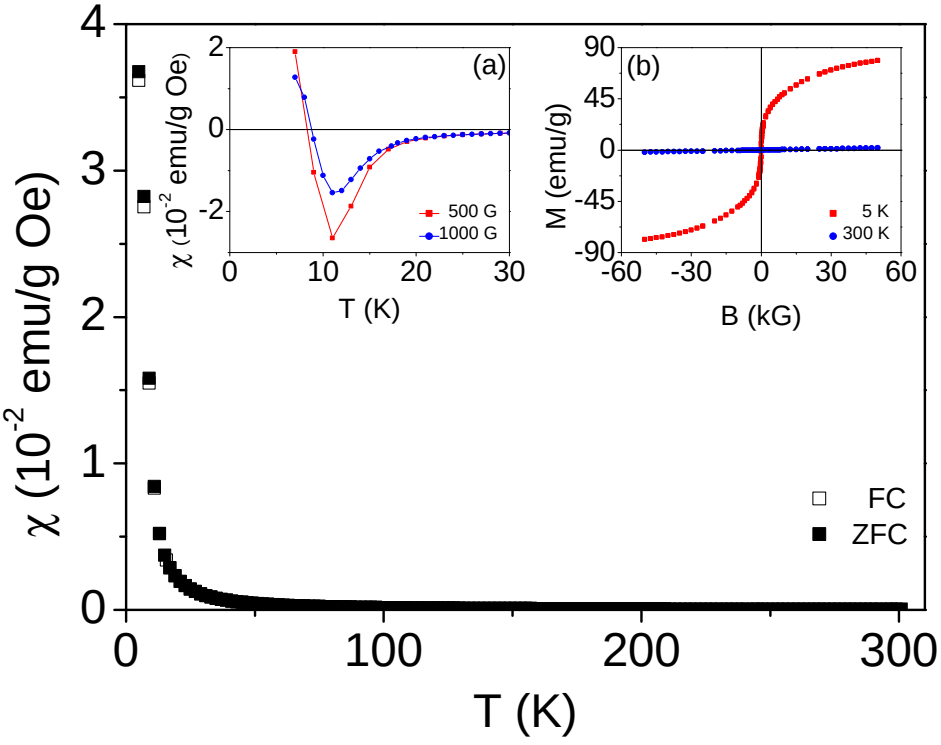

Fig. 5.8: ZFC (solid symbol) and FC (open symbol) susceptibility χ as a function of temperature T for 10% Al doped α nickel hydroxide. Inset (a) shows $\frac{d(\chi T)}{dT}$ as a function of temperature T and (b) shows M-B loops at 5 and 300 K.

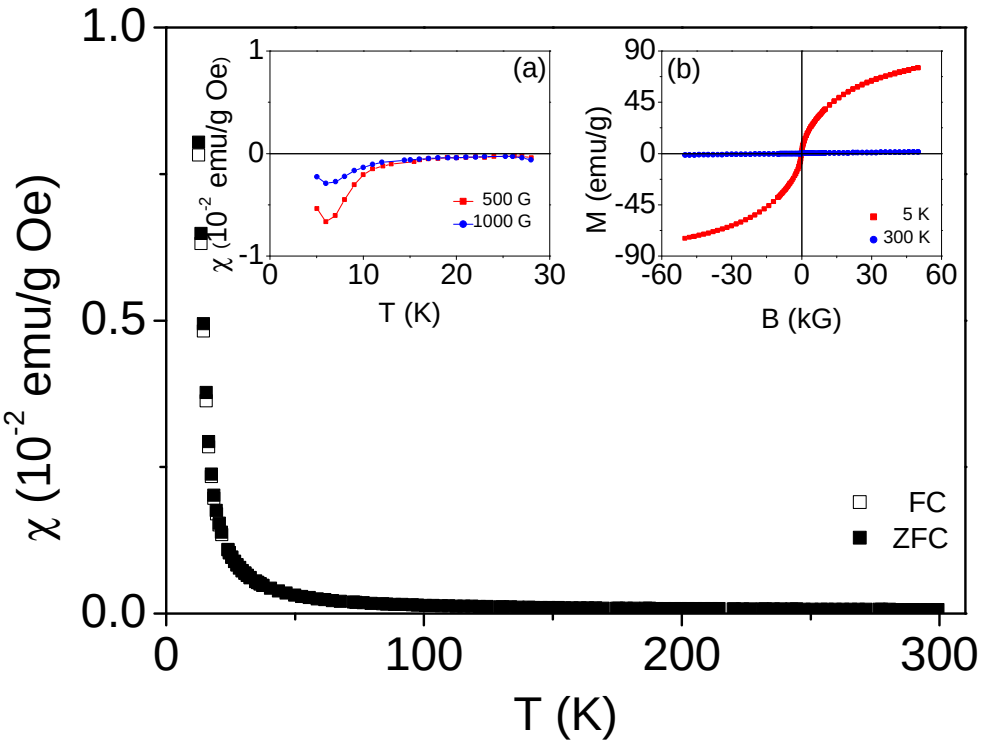

Fig. 5.9: ZFC (solid symbol) and FC (open symbol) susceptibility χ as a function of temperature T for 20% Al doped α nickel hydroxide. Inset (a) shows $\frac{d(\chi T)}{dT}$ as a function of temperature T and (b) shows M-B loops at 5 and 300 K.

differ and so it must be kept in mind while comparing saturation magnetization of three samples. Magnetic field of 50 kG at 5 K is again not found sufficient to saturate the system. In fact, such systems require much higher magnetic fields at further lower temperatures to achieve saturation [36]. The ZFC susceptibility versus temperature data on Al doped α nickel hydroxide are fitted to Eq. (5.2). Figure 5.6 shows the data and resulting fits. Estimated values of parameters μ and J_1 are shown in Table 5.1. This table also shows values of molecular weight, exchange interaction energy J_2 and g-factor. The exchange constants J_1 and J_2 are seen to decrease with increasing concentration of dopant. Because of this, the Curie transition temperature decreases with increasing concentration of Al^{3+} ions in the lattice of α nickel hydroxide.

5.3 Conclusion

In this Chapter, behavior of undoped, 10 and 20% Al doped samples of alpha nickel hydroxide nanoparticles are reported. Samples are found to undergo ferromagnetic transitions at lower temperatures. The corresponding Curie transition temperatures are seen to decrease with increasing concentration of Al in the lattice.

Chapter 6

BETA NICKEL HYDROXIDE NANOPARTICLES

In this chapter structural, thermal and magnetic characterization of beta nickel hydroxide nanoparticles are discussed.

6.1 Structural Characterization

Room temperature XRD patterns of synthesized sample is shown in Fig. 6.1. The pattern confirms the formation of single phase β nickel hydroxide [35]. Broadening in the peak indicates for nanocrystalline nature of sample. Average crystallite size, using Scherrer formula, comes out to be about 7 nm. Values of lattice parameters a and c of hexagonal unit cell are estimated to be 3.08(1) and 4.6(1) $\mathring{A}$ respectively.

FTIR spectra of the sample is shown in Fig. 6.2. Various observed bands are assigned as follows [35]. The sharp 3640 cm^{-1} band is assigned to free ν_{O-H} stretching in the OH group, broad band centered around 3440 cm^{-1} is due to absorbed water, the 1635 cm^{-1} band is due to δ_{H_2O} bending from absorbed water, 1385 cm^{-1} is due to Ni-O stretching, 525 cm^{-1} band is due to δ_{O-H} bending in the O-H group and 465 cm^{-1} band is due to Ni-O bending. This analysis yields the chemical formula of the sample as $Ni(OH)_2 \cdot nH_2O$. Origin of band at 1000 cm^{-1} is not clear. This band of unknown origin has been also observed by others [35].

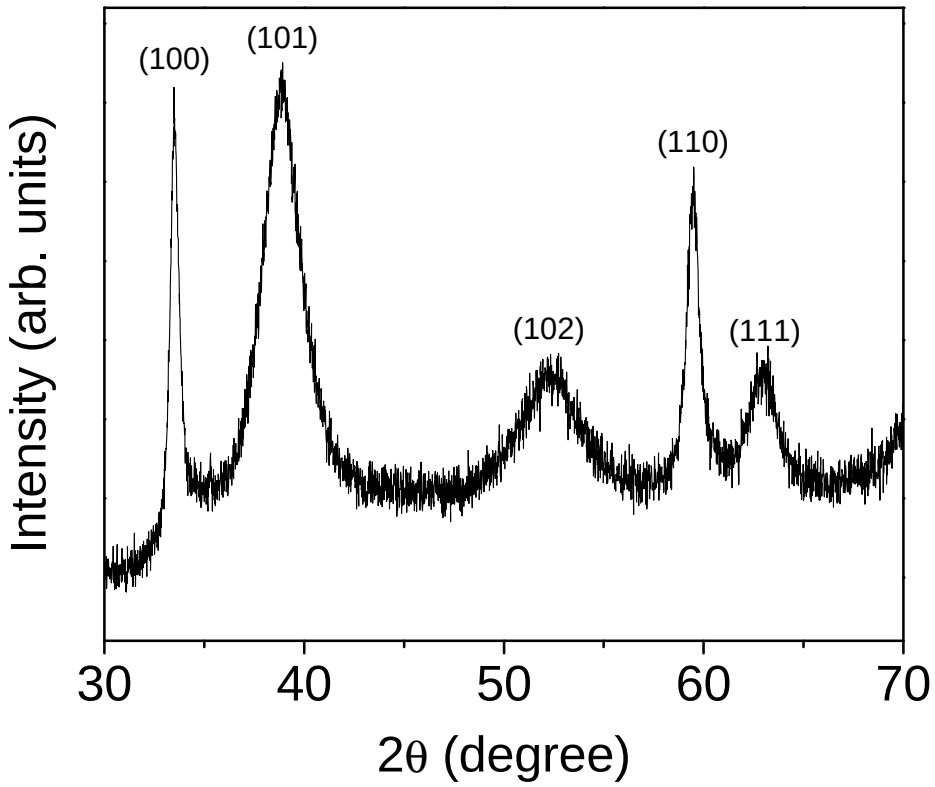

Fig. 6.1: Room temperature x-ray diffraction pattern of β nickel hydroxide nanoparticles.

The sample is also characterized with thermogravimetric analyzer to estimate the value of n. In this, mass of sample is measured while being heated in air at a constant rate. Figure 6.3 shows TGA curve for synthesized sample. It decomposes to NiO on heating in air. In this decomposition, the sample undergoes a mass loss of 25.34%. This analysis yields the molecular formula of sample to be $Ni(OH)_2 \cdot nH_2O$ with $n = 0.41$.

6.2 Magnetization

6.2.1 Temperature dependence

Figure 6.4 shows ZFC and FC susceptibility χ versus temperature T for the β nickel hydroxide nanoparticles in presence of 500 G applied magnetic field. Both ZFC and

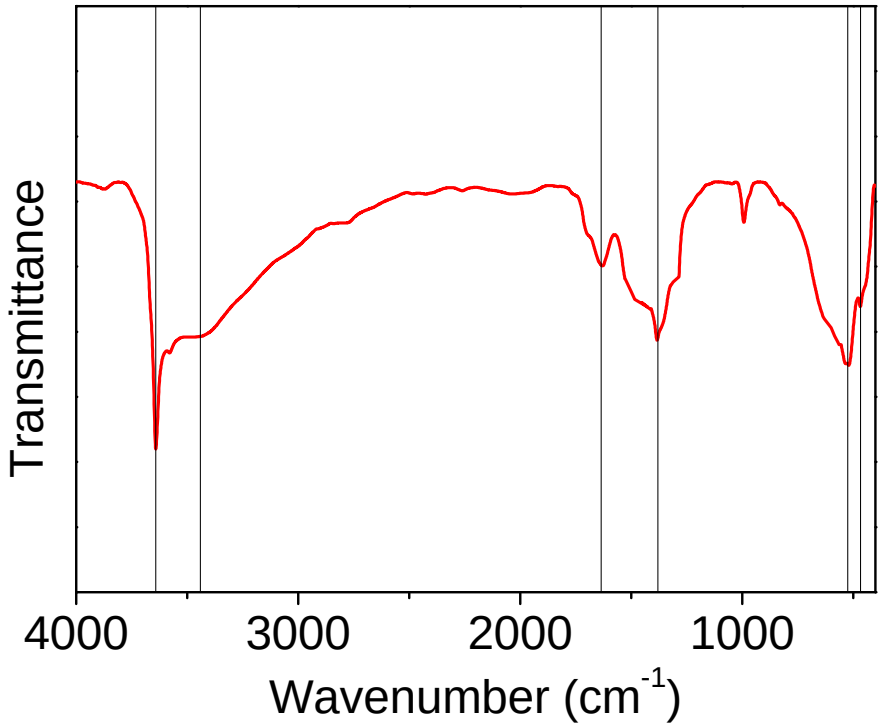

Fig. 6.2: FTIR spectra of β nickel hydroxide at room temperature.

FC susceptibility decrease with increasing temperature following the same path at higher temperatures. However, both curves are seen to bifurcate at lower temperature. Inset (a) shows magnified view of ZFC and FC data in different applied magnetic fields. These curves always bifurcate at 21(2) K. In other words, the bifurcation temperature T_{bf} is found to be independent of the strength of applied magnetic field. Therefore, the behavior of the system is not superparamagnetic. In fact, this bifurcation temperature represents the Néel transition temperature of the system.

Above a transition temperature θ, the magnetic susceptibility of ferro and antiferromagnetic materials is described by the Curie-Weiss law $\chi = \frac{C}{T-\theta}$. The parameter θ has a positive value for ferromagnetic interaction and has a negative value for antiferromagnetic interaction. In this way, one can characterize the nature of possible magnetic interaction in the system. Linear portion of χ^{-1} vs. T curve should be fitted

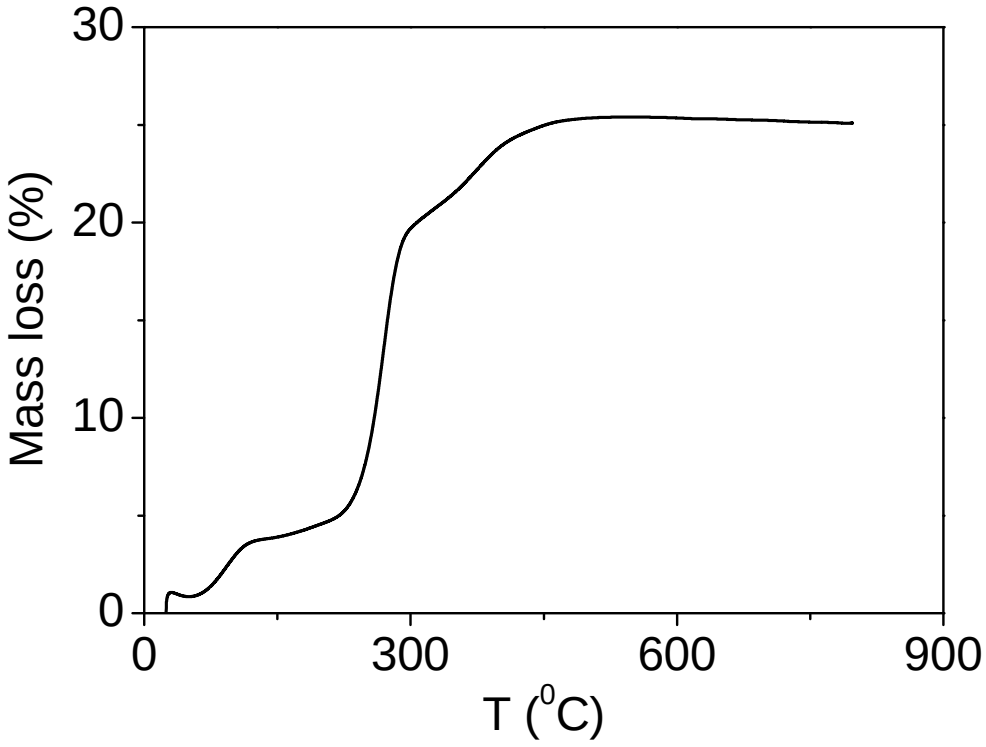

Fig. 6.3: Mass loss as a function of temperature for β nickel hydroxide.

to a straight line to estimate values of parameters C and θ.

Crystal structure of β nickel hydroxide is hexagonal [35]. In such materials, three exchange interactions J_1, J_2 and J_3 are present. Here J_1 represents strength of ferromagnetic exchange interaction among Ni^{2+} ions lying in hexagonal layers whereas J_2 and J_3 represent strength of possible antiferromagnetic interactions among Ni^{2+} ions lying in neighboring hexagonal layers. Inset (b) in Fig. 6.4 shows a plot of inverse susceptibility versus temperature. Linear portion of this plot is fitted to a straight line. This fit is shown as a solid line. From this fit, values of parameters C and θ are estimated to be 0.0115(2) emu K/g Oe and 22.5(3) K respectively.

Value of spin quantum number S, orbital angular momentum quantum number L and total angular momentum quantum number J for Ni^{2+} ion are 1, 3 and 4 respectively [1]. Theoretical values for spin magnetic moment and total magnetic moment for Ni^{2+}

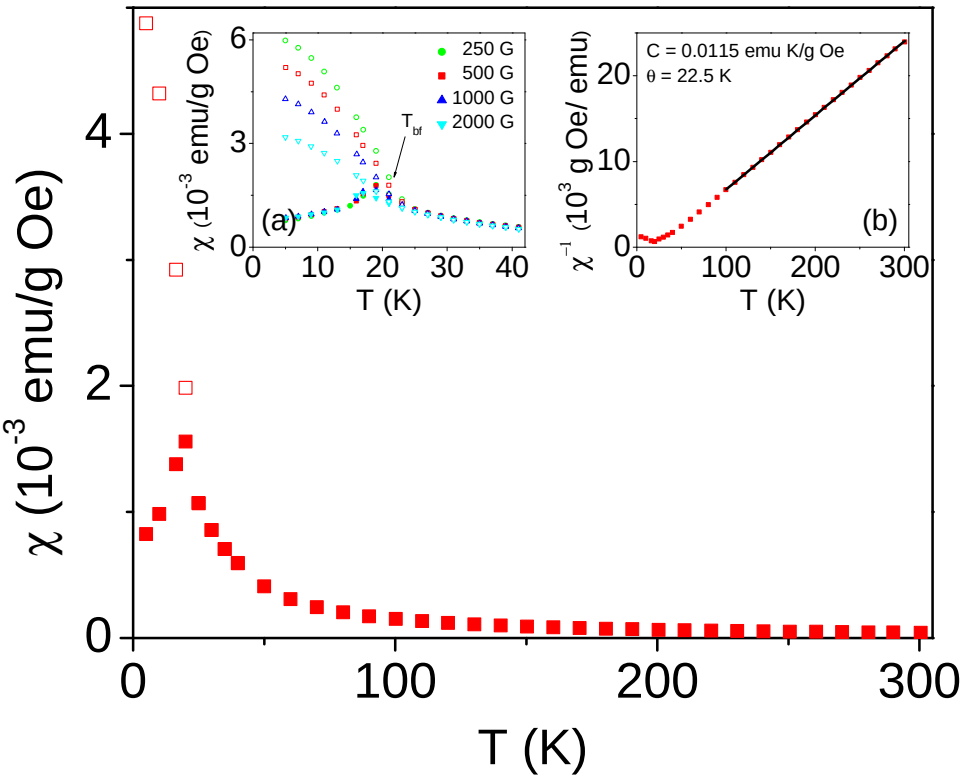

Fig. 6.4: Zero field cooled (solid symbol) and field cooled (open symbol) susceptibility χ as a function of temperature T for β nickel hydroxide nanoparticles in 500 G applied magnetic field. Inset (a) shows magnified view of data at lower temperatures in different applied magnetic fields. Inset (b) shows plot of χ^{-1} as a function of temperature in 500 G applied magnetic field.

ion turn out to be 1.41 and 4.47 μ_B respectively. The actual magnetic moment of the ion will depend on extent of quenching of orbital angular momentum in the system. In Curie-Weiss law, the value of parameter C is $\frac{N\mu^2}{3k_B}$, where N and k_B are number of Ni^{2+} ions per unit mass and the Boltzmann constant respectively. Using the estimated value of parameter C, the value of magnetic moment μ for Ni^{2+} ions in the sample turns out to be 3.03 μ_B. Somewhat similar values for ionic magnetic moment are also reported by others [35]. It is worth mentioning here once again that the parameter θ in Curie-Weiss law does not represent actual Curie temperature or Néel temperature

of a system if more than one type of magnetic interactions are present [35].

From Curie-Weiss law one gets [35]

$$\frac{d(\chi T)}{dT} = -\frac{C\theta}{(T-\theta)^2}. \tag{6.1}$$

From this equation it is clear that in a plot of $\frac{d(\chi T)}{dT}$ versus temperature T one should obtain a negative minimum at Curie temperature for a ferromagnetic transition and a positive maximum at Néel temperature for an antiferromagnetic transition. Figure 6.5 (a) shows a plot of χT versus temperature T for β nickel hydroxide nanoparticles in different applied magnetic fields. Figure 6.5 (b) shows a plot of $\frac{d(\chi T)}{dT}$ versus temperature T. In this plot a negative minimum at $T_1 = 23(2)$ K and a positive maximum at $T_2 = 17(2)$ K are seen. So, β nickel hydroxide nanoparticles undergo a two dimensional ferromagnetic ordering at 23(2) K and a three dimensional antiferromagnetic ordering at 17(2) K. It is also seen that both transition temperatures are independent of applied magnetic field strength.

In β nickel hydroxide, the Ni^{2+} spins in antiferromagnetic state are parallel to the c-axis within each c plane with alternate c planes aligned antiferromagnetically. The Hamiltonian of the system, considering the Ising model, is given by

$$\mathcal{H} = -2\sum_{i,j} J_{ij}\vec{S}_i \cdot \vec{S}_j. \tag{6.2}$$

Equations for θ and T_N are [35]

$$3k_B\theta = 2S(S+1)[J_1Z_1 + J_2Z_2 + J_3Z_3] \tag{6.3}$$

and

$$3k_BT_N = 2S(S+1)[J_1Z_1 - J_2Z_2 - J_3Z_3], \tag{6.4}$$

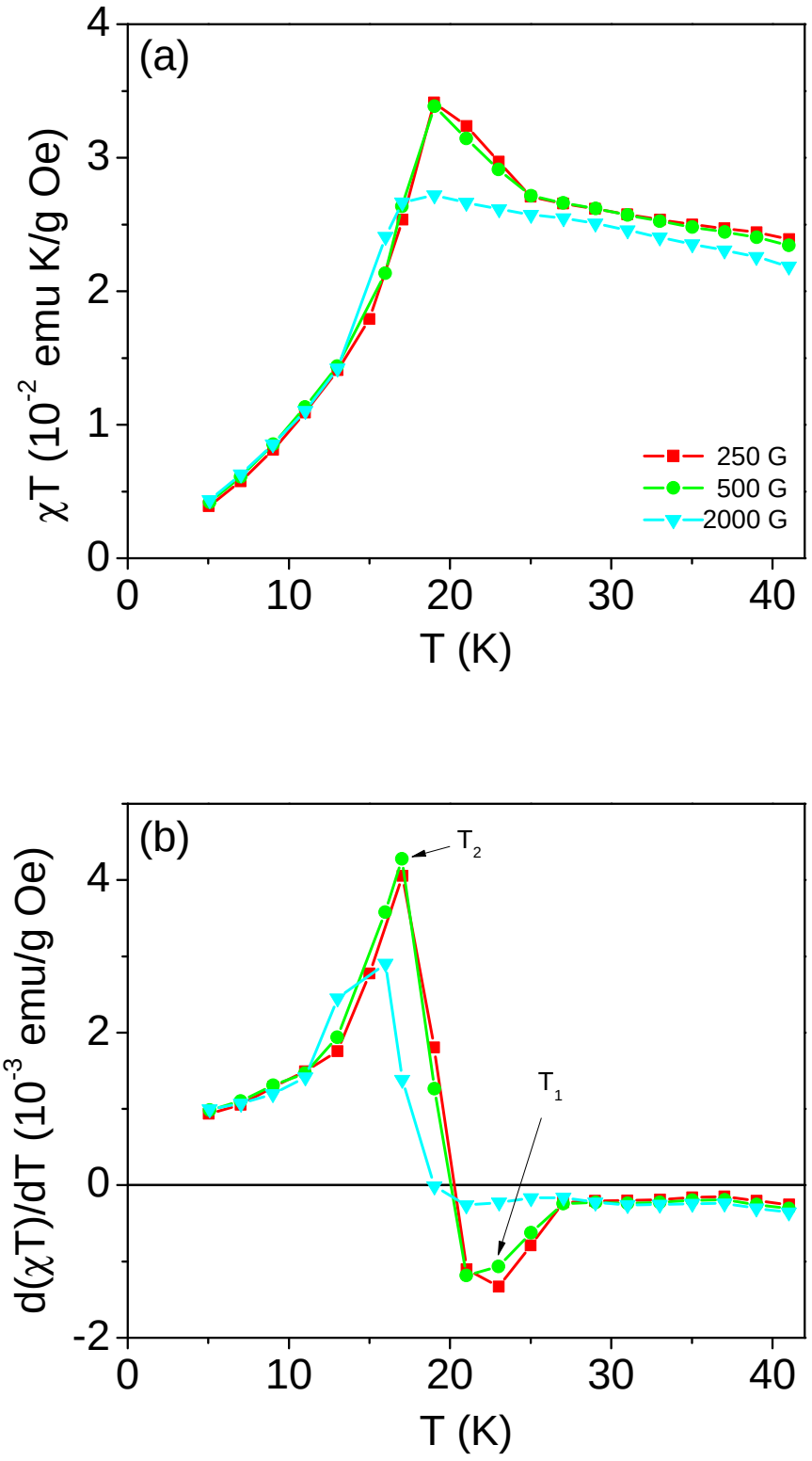

Fig. 6.5: (a) χT as a function of temperature T for β nickel hydroxide nanoparticles in different applied magnetic fields. (b) $\frac{d(\chi T)}{dT}$ as a function of temperature T.

where k_B is the Boltzmann constant. Here $Z_1 = 6$, $Z_2 = 2$ and $Z_3 = 12$ are the appropriate number of neighbors involved in the exchange constants J_1, J_2 and J_3 respectively for the hexagonal lattice [35]. Also $J_2 = 3\ J_3$. For present system, $\theta =$ 22.5(3) K, $T_N = 23(2)$ K (the temperature at which two dimensional ordering sets in) and $S(S+1) = 2$. From Eqs. (6.3) and (6.4) values of exchange constants J_1, J_2 and J_3 turn out to be about 2.84, -0.03 and -0.01 K respectively. Here, the exchange constant J_1 has a positive value and exchange constants J_2 and J_3 have negative values. Also, the magnitude of J_1 is largest. This analysis indicates that the intraplaner exchange interaction among Ni^{2+} ions is ferromagnetic in nature and is stronger than two interplaner antiferromagnetic interactions.

6.2.2 Field dependence

Magnetization of β nickel hydroxide nanoparticles versus applied magnetic field is also measured at 5 and 300 K. These measurements are shown in Fig. 6.6. This figure shows that at 300 K the magnetization of system increases linearly with increasing strength of applied magnetic field as per expectation in paramagnetic region. At 5 K, the magnetization initially increases with increasing strength of applied magnetic field followed by a sudden rise in the magnetization at higher magnetic fields. Inset in Fig. 6.6 shows a plot of $\frac{dM}{dB}$ versus applied magnetic field B. In this plot two peaks at magnetic fields $B_{C1} \approx 30$ kG and $B_{C2} \approx 55$ kG are seen. Similar behavior has also been observed for β nickel hydroxide nanoparticles [35]. The peak at B_{C1} is attributed to the switching of spins lying on the surface of particles from antiparallel orientation to a direction parallel to the applied magnetic field. The system undergoes a magnetic field induced transition, also known as metamagnetism, from antiferromagnetic to ferromagnetic order at B_{C2}. This magnetic field induced transition is also evident from the behavior of M vs. B curve at 5 K at higher magnetic fields. Also $B_{C2} \approx 2\ B_{C1}$, as per expectation [35]. The saturation magnetization M_S of a ferromagnet near

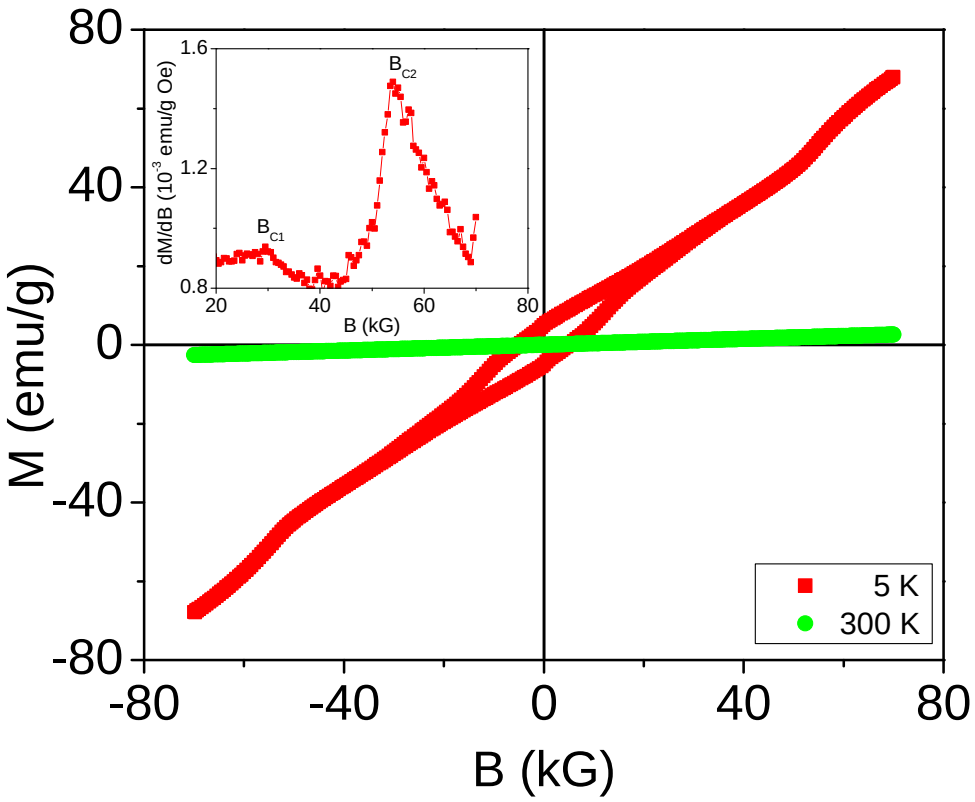

Fig. 6.6: M-B loops at 5 and 300 K for β nickel hydroxide nanoparticles. Inset shows a plot of $\frac{dM}{dB}$ as a function of applied magnetic field B at 5 K.

0 K is given by $M_S = NgS\mu_B$. For our sample of β nickel hydroxide particles, using $g = 2.14$ and $S = 1$ yields the calculated $M_S = 119$ emu/g. From this value and Fig. 6.6, one finds that a magnetic field of 50 kG at 5 K is not sufficient to saturate the system. In fact, such systems require magnetic field of few hundred kilogauss strength for saturation at low temperatures [35].

6.3 Conclusion

In this chapter, behavior of 7 nm β-$Ni(OH)_2 \cdot 0.4H_2O$ particles is discussed. This system has three exchange interactions among Ni^{2+} ions. The intraplaner exchange interaction is found to be ferromagnetic in nature. This interaction is seen to dominate over two weaker interplaner antiferromagnetic exchange interactions. The system is also found to undergo a magnetic field induced transition from antiferromagnetic to ferromagnetic state at low temperature.

Chapter 7

CONCLUSIONS

Synthesis, structural, thermal and magnetic characterization of cobalt hydroxide and nickel hydroxide nanoparticles are presented in this thesis. Both materials exist in alpha and beta phases. These systems have layered hexagonal structure. The alpha phase is unstable. This phase is stabilized by doping the system with trivalent Al^{3+} ions. The beta phase of cobalt hydroxide and nickel hydroxide are stable systems. Any attempt to dope the beta phase with Al stabilizes the system into the alpha phase. Phase of all synthesized samples are characterized with room temperature x-ray diffraction. Values of lattice parameters a and c of hexagonal unit cell are estimated. Both phases mainly differer in value of lattice parameter c. The value of lattice parameter c for alpha phase is found to be about seven times to that of beta phase. Diffraction peaks are seen to be quite broad. This indicates for nanocrystalline nature of samples. Average crystallite sizes are calculated with modified Scherrer formula.

The alpha phase of cobalt hydroxide and nickel hydroxide nanoparticles contains intercalated anions between hexagonal layers. These anions are introduced during the synthesis process. It causes quite large spacing between hexagonal layers. On other hand, the beta phase of cobalt hydroxide and nickel hydroxide do not contain any anions between the hexagonal layers causing much smaller interlayer spacing. All samples are found to contain some surface absorbed water. Molecular formula of each sample is established with help of FTIR spectra and thermogravimetric analysis.

Magnetic properties of alpha cobalt hydroxide and nickel hydroxide nanoparticles are found to be almost similar. Both undoped and Al doped samples show paramagnetic behavior at room temperature. On cooling, samples undergo to ferromagnetic states. In this state, ionic spins in hexagonal layers align themselves along the *c*-axis. In this way, the alpha phase is overall a ferromagnet. The Curie transition temperature decreases with increasing concentration of Al in the lattice. Magnetic properties of beta cobalt hydroxide and nickel hydroxide nanoparticles are also found to be almost similar. But, this behavior is somewhat different from that of the alpha phase. Both samples, that is beta cobalt hydroxide and nickel hydroxide nanoparticles, are paramagnetic at room temperature. On cooling, spins in each hexagonal layer align themselves along same direction. But spins in neighboring layers are aligned opposite to each other so that the system is overall an antiferromagnet. The beta cobalt hydroxide and nickel hydroxide also undergo a magnetic field induced transition to ferromagnetic state at lower temperature.

Work presented in this thesis shows that magnetic behavior of cobalt hydroxide and nickel hydroxide is very interesting and strongly dependent on spacing between neighboring hexagonal layers containing Co^{2+} and Ni^{2+} ions. In future, one may try to gradually vary this spacing by incorporating other suitable anions or ligands between the hexagonal layers and study magnetic properties of such samples.

BIBLIOGRAPHY

[1] C. Kittel, *Introduction to Solid State Physics*, (Wiley India Pvt. Ltd., New Delhi, 2013).

[2] N.W. Ashcroft and N.D. Mermin, *Solid State Physics*, (Cengage Learning India Pvt. Ltd., Delhi, 2017).

[3] A.J. Dekker, *Solid State Physics*, (Macmillan Publishers India Ltd., Delhi, 2014).

[4] L.J. de Jongh and A.R. Miedema, Adv.Phys. **23**, 1 (1974).

[5] L.J. de Jongh, *Magnetic Properties of Layered Transition Metal Compounds*, (Kluwer Academic, Boston, 1990).

[6] H. Gleiter, J. of Applied Crystallography **24**, 79 (1991).

[7] A.S. Edelstein and R.C. Cammarata, *Nanomaterials: Synthesis, Properties and Applications*, (Institute of Physics Publishing, Bristol, 2002).

[8] G. Cao, *Nanostructures and Nanomaterials: Synthesis, properties and applications*, (Imperial College Press Publishing, London, 2004).

[9] I.S. Jacobs and C.P. Bean, in *Magnetism*, Vol.III edited by G. T. Rado and H. Suhl (Academic Press Inc., New York, 1963).

[10] S. Chikazumi, *Physics of Magnetism*, (Wiley, New York, 1964).

[11] M. Rasa, Eur. Phys. J. E **2**, 265 (2000).

[12] D.K. Bairwa , K.K. Upman and G. Kantak, International Journal of Engineering, Management & Sciences **2**, 14 (2015).

[13] C. Hanley, J. Layne, A. Punnoose, K.M. Reddy, I. Coombs, A. Coombs, K. Feris and D. Wingett, Nanotechnology **19**, 295103 (2008).

[14] K.V. Wong and O.D. Leon, Advances in Mechanical Engineering **2010**, 1 (2010).

[15] J.E. Contreras, E.A. Rodriguez and J. Taha-Tijerina, Electric Power Systems Research **143**, 573 (2017).

[16] R.W. Chantrell and K. O'Grady, in *Applied Magnetism* edited by R. Gerber, C. D. Wright, G. Asti (Kluwer Academic Publishers, The Netherlands, 1994).

[17] A. Akbarzadeh, M. Samiei and S. Davaran, Nanoscale Research Letters **7**, 144 (2012).

[18] B.S. Murty, P. Shankar, B. Raj, B.B. Rath and J. Murday, *Textbook of nanoscience and nanotechnology*,(Universities Press (India) Private Limited, Hyderabad, 2013).

[19] D. Sidorenko, P. Loginov, L. Mishnaevsky and E. Levashov, Materials **10**, 1171 (2017).

[20] A.A. Zaitsev, D.A. Sidorenko, E.A. Levashov, V.V. Kurbatkina, V.A. Andreev, S.I. Rupasov and P.V. Sevastyanov, Journal of Superhard Materials **32**, 423 (2010).

[21] C.L. Santos, A.J.R. Albuquerque, F.C. Sampaio, D. Keyson, in *Microbial pathogens and strategies for combating them: science, technology and education.* Vol. 4. (Formatex Research Center Badajoz, Spain, 2013) p. 143.

[22] Y.L. Zhao, J.M. Wang, H. Chen, T. Pan, J.Q. Zhang and C.N. Cao, Electrochim. Acta **50**, 91 (2004).

[23] A. Sugimoto, S. Ishida and K. Hanawa, J. Electrochem. Soc. **146**, 1251 (1999).

[24] Y.J. Leng, B. Liu, F.J. Wang, Y. Xiao and Z.F. Ma, Chin. J. Power Sources **24**, 326 (2000).

[25] J.D. Rall, M.S. Seehra, N. Shah and G.P. Huffman, J. Appl. Phys. **107**, 09B511 (2010).

[26] Z. Liu, R. Ma, M. Osada, K. Takada and T. Sasaki, J. Am. Chem. Soc. **127**, 13869 (2005).

[27] R.M. Dell, Solid State Ionics **134**, 139 (2000).

[28] T. Takada, Y. Bando, M. Kiyama, H. Miyamoto and T. Sato, J. Phys. Soc. Japan **21**, 2726 (1966).

[29] T. Takada, Y. Bando, M. Kiyama, H. Miyamoto and T. Sato, J. Phys. Soc. Japan **21**, 2745 (1966).

[30] A. Szytula, A. Murasik and M. Balando, Phys. Status Solidi B **43**, 125 (1971).

[31] S.D. Tiwari and K.P. Rajeev, Phys. Rev. B **77**, 224430 (2008).

[32] X.H. Liu, W. Liu, W.J. Hu, S. Guo, X.K. Lv, W.B. Cui, X.G. Zhao and Z.D. Zhang, J. Appl. Phys. **93**, 202502 (2008).

[33] P. Shamba, R. Zeng, J.Q. Wang and S.X. Dou, J. Appl. Phys. **107**, 09A919 (2010).

[34] J.R. Neilson, D.E. Morse, B.C. Melot, D.P. Shoemaker, J.A. Kurzman and R. Seshadri, Phys. Rev. B **83**, 094418 (2011).

[35] J.D. Rall, M.S. Seehra and E. S. Choi, Phys. Rev. B **82**, 184403 (2010).

[36] J.D. Rall and M.S. Seehra, J. Phys.: Condens. Matter **24**, 076002 (2012).

[37] L. Zhiwei, X. Xiang and T. Zongmin, Advanced Materials Research **347-353**, 3379 (2012).

[38] T.N. Ramesh and P.V. Kamath, Bull. Mater. Sci. **31**, 169 (2008).

[39] C. Rani, S.D. Tiwari and D. Kumar, IEEE Transactions on Magnetics **51**, 6001005 (2015).

[40] B.D. Cullity, *Elements of X-Ray Diffraction* (Addison-Wesley Publishing Company, Inc., USA, 1956).

[41] C.N. Banwell and E.M. McCash, *Fundamentals of Molecular Spectroscopy*, (Tata McGraw Hill, New Delhi, 2007).

[42] J.S. Gaffney, N.A. Marley and D.E. Jones, in *Characterization of Materials*, edited by E. N.Kaufmann (Wiley, New York, 2003).

[43] P. Gabbott, *Principles and Applications of Thermal Analysis* (Blackwell Publishing Ltd, UK, 2008).

[44] S. Foner, Rev. Sci. Instrum. **30**, 548 (1959).

[45] Z.A. Hu, Y.L. Xie, Y.X. Wang, L.J. Xie, G.R. Fu, X.Q. Jin, Z.Y. Zhang, Y.Y. Yang and H.Y. Wu, J. Phys. Chem. C **113**, 12502 (2009).

[46] J. Yang, H. Liu, W.N. Martens and R.L. Frost, J. Phys. Chem. C **114**, 111 (2010).

[47] J.P. Van Dyke and W.J. Camp, Phys. Rev. B **9**, 3121 (1974).

[48] R. Navarro in *Magnetic Properties of Layered Transition Metal Compounds*, ed. L.J. de Jongh (Kluwer Academic, Boston, 1990) p. 138.

[49] Z. Wang, M. Lee, E.S. Choi, J. Poston and M.S. Seehra, J. Magn. Magn. Mater. **407**, 83 (2016).

[50] W. Lotmar and W. Feitknecht, Zeitschrift fuer Kristallographie, Kristallgeometrie, Kristallphysik, Kristallchemie **93**, 368 (1936).

[51] X. Liu, C. Feng, F. Xiao, S.W. Or, Y. Sun, C. Jin and A. Xia, Materials Research **17**, 186 (2014).

[52] X.H. Liu, W. Liu, X.K. Lv, F. Yang, X. Wei, Z.D. Zhang and D.J. Sellmyer, J. Appl. Phys. **107**, 083919 (2010).

[53] F. Portemer, A. Delahaye-Vidal and M. Figlarz, J. Electrochem. Soc. **139**, 671 (1992).

[54] E.E. Bragg and M.S. Seehra, Phys. Rev. B **7**, 4197 (1973).

[55] T. Bitoh, K. Ohba, M. Takamatsu, T. Shirane and S. Chikazawa, J. Phys. Soc. Jpn. **64**, 1305 (1995).

PUBLICATIONS

In SCI Journals

1. *Nature of Magnetic Interactions in β-Co(OH)$_2$ Nanoparticles.*
   Anu Gupta, S. D. Tiwari and Devendra Kumar, Phys. Status Solidi B **253**, 1795 (2016).

2. *Magnetic Properties of Undoped and Al doped Layered α-Co(OH)$_2$.*
   Anu Gupta and S. D. Tiwari, Physica B **525**, 21 (2017).

In Conferences

1. *Thermal and Magnetic Characterization of Cobalt Oxyhydroxide Nanoparticles.*
   Anu Gupta and S. D. Tiwari, International Conference on Magnetic Materials & Applications (ICMAGMA 2015) held at VIT University, Vellore, India during December 02-04, 2015.

2. *Synthesis and Characterization of Cobalt Hydroxide Nanoparticles.*
   Anu Gupta and S. D. Tiwari, 2^{nd} Conference on Microscopy in Materials Science and 2^{nd} Annual Meeting of Academy of Microscope Science & Technology (AMST 2016) held at Thapar University, Patiala, India during February 25-27, 2016.

3. *Effect of Al Doping on Magnetic Behavior of layered α-Ni(OH)$_2$ Nanoparticles.*
   Anu Gupta and S. D. Tiwari, 4^{th} International Conference on Nanoscience and Nanotechnology (ICONN 2017) held at SRM University, Chennai, India during August 09-11, 2017.